Petascale Simulations of the Morphology and the Molecular Interface of Bulk Heterojunctions

Jan-Michael Y. Carrillo,[*,†,‡] Zach Seibers,[¶] Rajeev Kumar,[†,‡] Michael A. Matheson,[§] John F. Ankner,[‖] Monojoy Goswami,[†,‡] Kiran Bhaskaran-Nair,[⊥,#] William A. Shelton,[⊥,#] Bobby G. Sumpter,[†,‡] and S. Michael Kilbey,II[*,@]

†*Center for Nanophase Materials Sciences, Oak Ridge National Laboratory, Oak Ridge, TN 37831, USA*

‡*Computer Science and Mathematics Division, Oak Ridge National Laboratory, Oak Ridge, TN 37831, USA*

¶*Department of Energy Science and Engineering, University of Tennessee, Knoxville, TN 37996, USA*

§*National Center for Computational Sciences, Oak Ridge National Laboratory, Oak Ridge, TN 37831, USA*

‖*Spallation Neutron Source, Oak Ridge National Laboratory, Oak Ridge, TN 37831, USA*

⊥*Center for Computation and Technology, Louisiana State University, Baton Rouge, LA 70803, USA*

#*Cain Department of Chemical Engineering, Louisiana State University, Baton Rouge, LA 70803, USA*

@*Departments of Chemistry and Chemical and Biomolecular Engineering, University of Tennessee, Knoxville, TN 37996, USA*

E-mail: carrillojy@ornl.gov; mkilbey@utk.edu

Abstract

Understanding how additives interact and segregate within bulk heterojunction (BHJ) thin films is critical for exercising control over structure at multiple length scales and delivering improvements in photovoltaic performance. The morphological evolution of poly(3-hexylthiophene) (P3HT) and phenyl-C_{61}-butyric acid methyl ester (PCBM) blends that are commensurate with the size of a BHJ thin film is examined using petascale coarse-grained molecular dynamics simulations. Comparisons between 2 component and 3 component systems containing short P3HT chains as additives undergoing thermal annealing demonstrate that the short chains alter the morphology in apparently useful ways: They efficiently migrate to the P3HT/PCBM interface, increasing the P3HT domain size and interfacial area. Simulation results agree with depth profiles determined from neutron reflectometry measurements that reveal PCBM enrichment near substrate and air interfaces, but a decrease in that PCBM enrichment when a small amount of short P3HT chains are integrated into the BHJ blend. Atomistic simulations of the P3HT/PCBM blend interfaces show a non-monotonic dependence of the interfacial thickness as a function of number of repeat units in the oligomeric P3HT additive, and the thiophene rings orient parallel to the interfacial plane as they approach the PCBM domain. Using the nanoscale geometries of the P3HT oligomers, LUMO and HOMO energy levels calculated by density functional theory are found to be invariant across the donor/acceptor interface. These connections between additives, processing, and morphology at all length scales are generally useful for efforts to improve device performance.

Keywords

bulk hetrojunction, organic photovoltaics, petascale simulations, neutron reflectometry, molecular dynamics simulations, coupled cluster methods, donor/acceptor interface

The development of alternative and renewable sources of energy is essential because of the progressive depletion of fossil fuel-based non-renewable sources. Harnessing solar energy is particularly attractive because of its abundance, relatively low environmental impact and zero CO_2 emission. Polymer-based organic photovoltaic devices, or OPVs, based on the bulk heterojunction (BHJ) concept consisting of a blend of donor- and acceptor-type materials are a promising technology because these devices are made of more readily available materials and can be processed using high throughput methods that are scalable and less energy intensive than inorganic-based counterparts. However, understanding relationships between polymer design, BHJ morphology, and optoelectronic properties and accurately predicting the effects of these relationships on the power conversion efficiency (PCE) of the OPV device are major challenges that need to be addressed.[1–5]

Currently, the rational design of polymers that act as electron donors in OPVs is marred by difficulties originating in the complex interactions that govern miscibility, crystallization, and the formation of organic–organic and organic–inorganic interfaces in BHJ active layers comprising organic donor-type and fullerene-based electron acceptors that are sandwiched between the electrodes. The effects of polymer molecular weight, polydispersity and processing compound these difficulties. Despite this large parameter space, there is a general consensus that morphology plays a vital role in dictating the optoelectronic performance resulting from different mechanisms, such as charge generation, transport and recombination that occur in the device.

For this reason, maximizing the PCE through optimization of BHJ morphology and stabilizing the otherwise transient morphology of the donor/acceptor BHJ thin film is a significant, coupled challenge that has received considerable attention in the OPV community. A characteristic of most benchmark OPV systems is the development of an irregular vertical distribution of acceptor fullerenes in the BHJ device that arises from different miscibilities of the donor-type polymer and fullerene acceptor. This is thought to be a suboptimal morphology and, as a result, characterizing the fullerene distribution in BHJ-

like thin films made under different conditions or with different materials is fundamentally important.[6] Neutron reflectometry (NR)[7,8] and near-edge x-ray adsorption fine structure (NEXAFS) spectroscopy[9,10] have been used to characterize the non-uniform distribution of PCBM fullerenes along the axis orthogonal to the plane of the electrode confining a P3HT/PCBM BHJ active layer. For example, Germack *et al.*[10] showed that changing the substrate from poly(3,4-ethylenedioxythiophene) polystyrene sulfonate (PEDOT:PSS) mixture to a Nafion-based hole transport layer (HTL) changes the BHJ vertical distribution from PCBM-rich near the substrate to P3HT-rich. Analogous segregation behavior is also observed for poly[(9,9-dioctylfluorenyl-2,7-diyl)-co-5,5-4',7'-di-2-thienyl-2',1',3'-benzothiadiazole] (APFO-3)–PCBM blends: PCBM content is enriched near the silicon substrate, while the interface where a gold electrode was deposited is enriched with APFO-3 due to specific interactions between the thienyl groups in the APFO-3 chain and the gold surface.[11] More recent neutron reflectometry experiments concluded that PCBM enrichment at the film/substrate interface occurs regardless of the substrate's hydrophilicity.[12] The phenomenon of vertical phase separation in BHJ thin films has also been investigated through multiscale computer simulations. For example, Lee *et al.*[13] showed that vertical phase segregation of P3HT/PCBM blend depends on the electrode material and thermal annealing process.

A variety of approaches that include surface treatments,[10–12,14]high boiling point solvents that slow the rate of solvent evaporation,[15,16] and additives have been pursued to address the issue of vertical phase segregation in P3HT/PCBM BHJs. Another promising route is the use of compatibilizers including C_{60} fullerenes derivatized with thiophene units that act like surfactants,[17–20] or block copolymers containing polythiophene blocks, such as polyethylene oxide (P3HT-b-PEO),[21] polyisoprene (P3HT-b-PI),[22] and polystyrene (P3HT-b-PS).[23] In general, these polymeric surfactants have been shown to improve PCE at low loading, but phase separation at higher loading leads to a decrease in OPV performance.[21,23] To understand these outcomes, the influence of block copolymer compatibilizers on the domain sizes

and interfacial morphological characteristics of the morphological structures of semiflexible polymer–fullerene blends such as P3HT/PCBM blends was recently investigated using computer simulations by Kipp and Ganesan.[24] These simulations demonstrated that block copolymer (BCP) composition is one of the parameters that can tune morphologies and interfacial characteristics in BHJ blends. The strategy of using compatibilizers is meant to lower the P3HT/PCBM interfacial tension, which may result in smaller domains, but could also have the unintended consequence of affecting the vertical phase segregation of fullerenes in the BHJ–substrate morphology.

Alternatively, it is possible to influence the morphology of the BHJ by adding low molecular weight (MW) polymers. The concept of influencing morphology with a simple low MW P3HT additive is promising because it provides a cost-effective solution that requires no additional manufacturing processes—it does not require additional synthesis steps to synthesize complex compatibilizers or to introduce chemically dissimilar additives. Recent results based on large scale coarse-grained molecular dynamics simulations for a P3HT/PCBM BHJ reveal that for short oligomeric P3HT chains ($N = 10$), the BHJ exhibits a macrophase separated morphology having layered and aligned P3HT chains.[25] Interestingly, these systems exhibit higher interfacial surface area-to-volume ratios that are thought to arise from the partial miscibility of the short chains with the PCBM phase. In the present work, we build on these efforts by incorporating substrates and introducing small amounts of short-chain P3HT polymers as an additive that is blended with longer P3HT chains and PCBM fullerenes to make a BHJ film. We expect that these short-chain additives will influence film morphology through two distinct mechanisms: (i) Mixing of short P3HT chains into the blend will swell the P3HT domains, and (ii) interfacial tension may decrease due to the migration of short P3HT chains to the donor-acceptor interface where they are partially miscible. We also expect that the short chains will affect the BHJ film/substrate interface because short chains have higher diffusional mobility and the capacity to pack better when adsorbed, because of their smaller size. Each of these effects should depend on the quantity of short chains added to the system.

In order to probe the effect of short P3HT chains on BHJ morphology, our strategy is to couple petascale simulations with neutron reflectometry studies. Petascale computing refers to calculations done in excess of one quadrillion floating-point operations per second, suiting it for this challenging scientific problem. We harness the resources available at one of the US Department of Energy's Leadership Computing Facilities (LCF)[26] and employ petascale and multiscale computational approaches using coarse-grained molecular dynamics simulations, atomistic molecular dynamics simulations and density functional theory calculations. Such an approach minimizes finite size effects and non-convergence of simulation results and also ensures adequate sampling statistics. Our computational strategy, which is mirrored in how this *Article* is laid out, is illustrated in Figure 1. First, we discuss the results of coarse-grained simulations of bulk and thin film systems (having substrates), investigating the effect of low MW additives on the morphology of the BHJ. Then we compare these results with structural description of BHJ obtained from neutron reflectivity measurements. Second, we conduct atomistic simulations of the electron donor/electron acceptor interface by representing the interface between the P3HT and PCBM domains as a slab of PCBM and P3HT oligomers with full atomistic details in order to investigate the sharpness of the interface and the orientation of the thiophene rings. Finally, we sample the geometries of the P3HT oligomers across the interface and use density functional theory (DFT) and higher fidelity coupled cluster methods (CC) to calculate the LUMO and HOMO levels as a function of location at the interface. In aggregate, these studies provide a clear picture that captures how morphology at all length scales scales as well as electronic structure at the donor/acceptor interface are impacted by the addition of short P3HT chains.

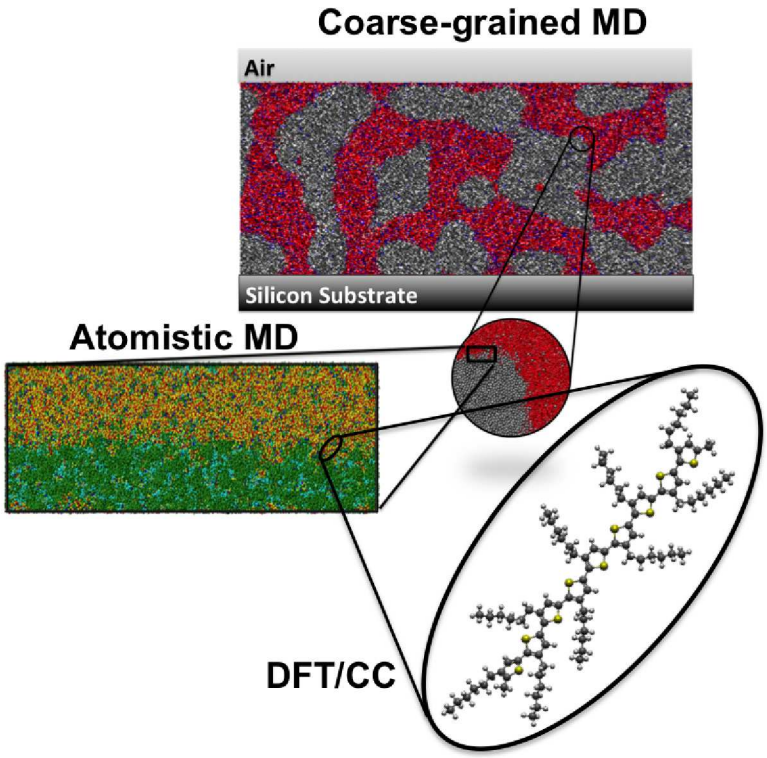

Figure 1: Schematic of the different levels of theory, modeling and simulation implemented using petascale computation used to model the active layer of a bulk heterojunction. (Not drawn to scale.) A set of coarse-grained potentials for P3HT/PCBM is used to perform classical molecular dynamics simulations over length and time scales matching the thermal annealing of thin films. The insight gained from the coarse-grained MD was used to design the full-atomistic simulation at the interfaces between P3HT chains and PCBM fullerenes in order to obtain more precise information on the orientation of the electron donor at these interfaces. From this information, a quantum density functional theory and coupled cluster method (DFT/CC) calculations are used to determine the electronic structure.

Results and Discussion

Bulk and thin film morphology of BHJ systems *via* petascale simulations and reflectivity measurements

Coarse-grained molecular dynamics (CGMD) simulations were performed using the P3HT-PCBM coarse-grained force field developed by Lee, Pao and Chu (LPC).[27] The simulations were run using LAMMPS[28] with GPU acceleration[29] in the Oak Ridge Leadership Computing Facility (OLCF) supercomputer Titan. The details of the implementation of the simulations are similar to those described by Carrillo *et al.*,[25] but there are distinct differences that merit illumination. First, we emphasize that these are large systems having thicknesses of the P3HT:PCBM mixture commensurate with those used as the active layers of P3HT:PCBM organic photovoltaic devices and areal dimensions ($L_x \times L_y$) 10.6 times larger than the size previously studied by Carrillo *et al.*[25] This simulation system is both an order of magnitude larger in size and longer in timescale than the recent coarse-grained simulations conducted by Lee *et al.*[13] Second, and similar to the work of Lee *et al.*,[13] bounding substrates are explicitly considered in studies of thin film systems. The impact of these features is two-fold: The longer timescales of the simulations provide clarity as to whether system achieves equilibrium, and the (relatively) large L_x and L_y sizes are necessary to obtain sufficient statistics in the xy-plane such that z-resolved volume fractions are appropriate for comparing results from neutron reflectometry measurements, which are made over a macroscopic sample. A snapshot of the simulation showing the simulation box configuration, orientation and dimensions is shown in Figure S.1 in the *Supporting Information*.

For our simulation studies of thin film systems, the parameterization of the substrate–BHJ interactions used in the CGMD is based on the NR experiments by Kiel *et al.*,[7] which show that for a BHJ thin film of 1:1 weight ratio of P3HT:PCBM in contact with a silicon wafer substrate, the volume fraction of PCBM near the silicon wafer interface is $\sim 75\%$. Unlike the bottom substrate, the top substrate—representing the air/BHJ interface—is com-

posed of purely repulsive Lennard-Jones beads. This naturally mimics the experimental situation, and the rationale for employing an athermal wall for the air/BHJ interface is because entropic effects dominate in the interfacial region between air and the blend. More details of the simulation methodology are presented in the *Supporting Information*.

To study the effect of short P3HT chains as a low MW additive on the vertical distribution of PCBM in the active layer of a P3HT:PCBM BHJ, we simulated four systems with $N_l = 100$ and $N_s = 10$, where N_l and N_s are the degrees-of-polymerization of the long and short P3HT chains, respectively. The overall P3HT:PCBM weight ratio is maintained at 1:1 while the weight percentage of the short chains is systematically varied from $\phi_a = 0$ to 10% (the subscript "a" is chosen to represent "additive"). In each of the four systems, there are constant numbers of PCBM and P3HT beads, and the main difference among the four systems simulated is in how the bonds between the 3-hexyl thiophene repeat units are distributed. This difference is reflected in the values of m_l and m_s, which are the number of long and short P3HT chains, respectively (see Table S.1 in the *Supporting Information*). In so doing, we expect that the differences in properties among the four systems could be attributed to entropic effects. For comparison purposes, we also simulated systems containing short and long P3HT chains with PCBM in the absence of bounding substrates to mimic the configuration of bulk systems. The make-up of these systems, which allow bulk and thin film systems to be compared, is detailed in Table S.2 in in the *Supporting Information*.

Figure 2 illustrates the effect of adding short chains on the morphology of the bulk systems as a function of ϕ_a. The snapshots show that as the proportion of short chains increases in the BHJ blend in the bulk systems, the short-chains intermix with the PCBM domain. In the limit where only short-chains are present in the blend, shown as $\phi_a = 100\%$ in Figure 2—where the snapshot is generated based on results from previous simulations by Carrillo *et al.*[25]—the simulation results show that there is a phase separated morphology consisting of a mixed domain of PCBM and P3HT chains and another domain that is predominantly ordered P3HT chains. This finding is similar to what is observed in experiments by Russell

et al.[30] where it was shown that when mixed with PCBM, low molecular weight P3HT chains readily crystallize and promote a macrophase separated morphology. In the absence of PCBM, lower molecular weight P3HTs have higher degrees of crystallinity,[31,32] suggesting improved packing of polymer segments.

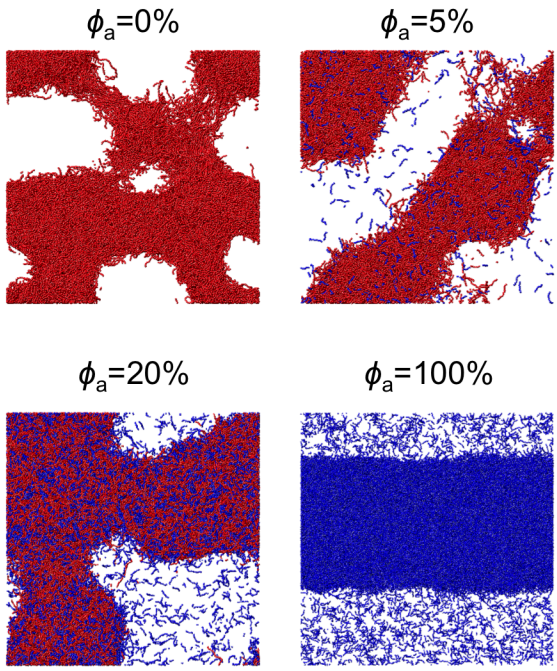

Figure 2: Cross-section of snapshots of the CGMD simulations in the bulk configuration with $\phi_a = 0\%$, 5%, 20% and 100% at $t = 400$ ns. Red beads are the monomers belonging to long P3HT chains ($N_l = 100$), blue beads belong to short P3HT chains ($N_s = 10$), and voids (white areas) denote the location of the PCBM domains.

It is germane to comment on this behavior and relate it to the recent experimental results of Russell *et al.*[30,33,34] In those works, it was argued that the origin of the phase-separated morphology is not demixing but rather, segregation of PCBM forced by the crystallization of P3HT. This view is contrary to the interpretation by Wu *et al.*,[35] who suggested that the annealing process is characterized by a competition between the mechanisms of slow polymer crystal growth and the faster growth of PCBM aggregates that leads to growth confinement that limits the size of P3HT and PCBM domains. Both mechanisms would lead to a phase separated morphology that qualitatively agrees with the simulation results; however, the

picture presented by Russell *et al.*[30,33,34] is more consistent with what we observed for the $\phi_a = 100\%$ system, where the entropic effect of the alignment of persistent segments—or the number of segments comprising the persistence length of a semiflexible polymer—drives the PCBM molecules away from the aligned P3HT segments comprising the chain. In contrast, the results by Wu *et al.* suggesting that better aligned P3HT lamella are caused by PCBM aggregates confining the P3HT chains[35] is consistent with what we observe for the $\phi_a = 0\%$ system, where the chains are more coil-like, as opposed to being rod-like in the $\phi_a = 100\%$ system. The improved P3HT alignment for a P3HT:PCBM BHJ at 1:1 total weight ratio and $\phi_a = 0\%$ is evidenced by the higher value of the average order parameter S as compared to that for a pure P3HT ($N = 100$) system, as shown in Figure S.2 in the *Supporting Information*.

One of the limitations of the coarse-grained model is that it does not incorporate the anisotropic, enthalpic π–π interactions that drive aligned polymers to crystallize. This detail is lost because of the nature of the LPC force-field, which coarse-grains the chain and represents a P3HT monomer as a single Lennard-Jones bead. The combination of bond, angle and dihedral interactions defined in the force-field make the polymer chain stiff, allowing it to behave like a semiflexible polymer. As a result, in this model, chain alignment occurs when the persistent segments of the semiflexible chains align because of entropic effects—it is easier to align stiff chains than coils. The LPC force-field also specifies that the interaction strength of the isotropic and attractive interaction between P3HT monomers is stronger than that of P3HT-PCBM bead interaction, facilitating the aggregation of the aligned P3HT segments. Despite the loss in detail of the π–π interaction, the model is able to capture the decrease in the miscibility of amorphous P3HT as a function of increasing degree-of-polymerization.[25]

The coarse-grained P3HT/PCBM simulation can be viewed as a polymer solution where the solvent molecules are the PCBM beads. Thus, we can employ the mean-field Flory-Huggins[36,37] (FH) model to describe the miscibility of P3HT in PCBM. In the FH framework,

the free energy of the polymer solution on a per lattice site basis consists of the entropy of binary mixing (per lattice site), $\Delta\bar{S}_{mix}$, and the energy of mixing (per lattice site), $\Delta\bar{U}_{mix}$. The FH parameter of PCBM and P3HT, χ_{12}, can be estimated from $\Delta\bar{U}_{mix}$ where,

$$\Delta\bar{U}_{mix} = \chi_{12}\phi_{\mathrm{PCBM}}(1-\phi_{\mathrm{PCBM}})k_B T \tag{1}$$

and ϕ_{PCBM} is the PCBM volume fraction. $\Delta\bar{U}_{mix}$ can be obtained from the simulations based on the change in the total pair-wise potential energy per lattice site after mixing P3HT chains with PCBM. In doing this, the lattice volume, v_o, is specified as the average Voronoi polyhedron volume in a simulation box comprising pristine PCBM.[25] In addition, it is possible to calculate the critical interaction parameter, χ_c:

$$\chi_c \approx \frac{1}{2} + \frac{1}{\sqrt{(N_{lattice})}} \tag{2}$$

where $N_{lattice}$ is the number of v_o volume units occupied by a P3HT chain with degree-of-polymerization, N such that:

$$N_{lattice} = N\frac{V_{\mathrm{3HT}}}{v_o} = \frac{4\pi r_{\mathrm{3HT}}}{3\eta_{\mathrm{P3HT}}}\frac{N}{v_o} \tag{3}$$

where V_{3HT} is the volume occupied by one coarse-grained P3HT bead monomer, r_{3HT} is the bead radius specified by the LPC force field and η_{P3HT} is the packing fraction of pure P3HT having a degree-of-polymerization, N. (Refer to the *Supporting Information* for details.) It should be appreciated that for a given $\phi_{\mathrm{PCBM}} < 1.0$, when $\chi_{12} > \chi_c$, there is a miscibility gap and the system will phase separate. We have found that by calculating χ_{12} and χ_c using this method applied to the simulation data reported by Carrillo *et al.*[25] for 1:1 PCBM:P3HT weight ratios and monodisperse P3HT chains having different values of N, the crossover point from miscibility to immiscibility ($\chi_{12} = \chi_c$) occurs at $N \approx 30$. The mean-field approach applied to the simulation data by Carrillo *et al.*[25] shows a decrease in the miscibility of amorphous P3HT as a function of the degree-of-polymerization, but the calculated crossover

value is shifted to higher values of N in comparison to simulations (immiscibility is already observed at $N = 25$) because the FH approach does not take into account the semiflexibility of the P3HT chains.

Recent experiments by Russell *et al.*[30] show that PCBM and amorphous P3HT are miscible, with values of χ_{12} increasing from 0.23 to 0.41 as P3HT molecular weight increases from 5 kDa to 48 kDa, which is consistent with the general criterion for miscibility of a binary mixture: $\chi_{12} < \chi_c = 0.5$. A similar trend is observed from contact angle measurements of spin-casted films in contact with water or ethylene glycol, where we estimated χ_{12} values of 0.34 and 0.39 for 5.6 kDa and 30 kDa, respectively. (See Table S.9 in the *Supplementary Information.*) However, the χ_{12} values obtained here by applying the FH framework to the simulation results by Carrillo *et al.*,[25] increase from 0.8 to 1.1, and χ_c values decrease from 1.26 to 0.71 as molecular weight increases from 2 to 25 kDa. Unlike the χ_{12} derived from experiments by Russell *et al.*,[30] the χ_{12} in simulations are greater than χ_c for some values of N, which indicates immiscibility of the binary mixtures for those N. The disagreement in the parameter used to gauge miscibility arises because the force-field used is coarse-grained and the χ_{12} calculation approach is mean-field. However, the essential finding of significance is that the simulations capture the correct trend of increasing χ_{12} as molecular weight increases. We note that Kozub *et al.*,[38] also reported immiscibility ($\chi_{12} = 0.86$) for a 50 kDa P3HT with a P3HT at a volume fraction of ∼0.6 P3HT, which is consistent with the simulation results. Further validation of the coarse-grained model was presented by Kumar *et al.*[39] who showed that PCBM is miscible for up to 14 vol% PCBM for N =100 (16.6 kDa) systems. This miscibility was confirmed by following the order and intensity of the peaks of the PCBM radial probability distribution function (RDF) as a function of PCBM volume fraction, which were extracted from simulation results. Higher order peaks began to develop for systems having PCBM volume fractions greater than 14%, indicating PCBM aggregation. This result agrees with recent experiments showing that PCBM is miscible in P3HT at PCBM volume fractions up to 15%-22% for P3HT molecular weights ranging from

50 to 90 kDa.[40,41] We emphasize that validating the accuracy of coarse-grained force fields, such as the LPC, by comparing with experimental results of neat components and blends is not trivial. Hence, we expect to only observe qualitatively similar trends with experiments and a direct mapping with experimental results is unfeasible.

The miscibility of the donor-type polymer and acceptor fullerene influences the BHJ morphology, which in turn affects the size of the domain formed by electron donor, d. It is often concluded that the domain size should be of the same order as the exciton diffusion length, nominally 10 nm, so that electron and hole recombination is minimized. Because charge separation mainly occurs at the P3HT/PCBM interface,[42] a complementary parameter that is equally important is the interfacial area-to-volume ratio, γ. Both d and γ are related to the P3HT volume fraction, ϕ_{P3HT}, as $\gamma \approx \phi_{\mathrm{P3HT}}(1-\phi_{\mathrm{P3HT}})/d$ for systems having smooth interfaces between the phases.[43] The domain size d of the additive-containing bulk systems is determined by fitting the spatial correlation function $g(r)_{\mathrm{P3HT-P3HT}}$ with a functional form of[44]

$$g(r)_{\mathrm{P3HT-P3HT}} = 1 + \frac{d}{2\pi r}\exp\left(-\frac{r}{\xi}\right)\sin\left(\frac{2\pi r}{d}\right) \tag{4}$$

which was calculated from CGMD simulation results and is shown in Figure 3(a). Here d is represented by the period of oscillation of Eq.4 at large values of r and ξ is the characteristic length of the spatial correlation function of Eq.4. Figure 3(b) shows that d obtained from fitting $g(r)_{\mathrm{P3HT-P3HT}}$ using Eq.4 increases as ϕ_a increases. We chose the data at 200 ns in presenting Figure 3(a), rather than at 400 ns, as that simulation time represents a near-equilibrium system[25] and because at 200 ns it is possible to identify one full oscillation in the spatial correlation function at all ϕ_a. The domain sizes obtained at 200 ns are approximately half their respective simulation box sizes (See Table S.2) and "finite size" effects are observed in calculating d when further coarsening of the domains occurs. Nonetheless, the trend of increasing d as a function of increasing ϕ_a holds for the different systems at $t > 200$ ns as well. In addition, the results of the $\phi_a = 0$ system presented in Figure 3(a-b) are consistent

with the results of the larger simulation by Carrillo *et al.*,[25] which had a box size of 100 nm, in comparison to the 66 nm box size used to generate the results presented in Figure 3(a).

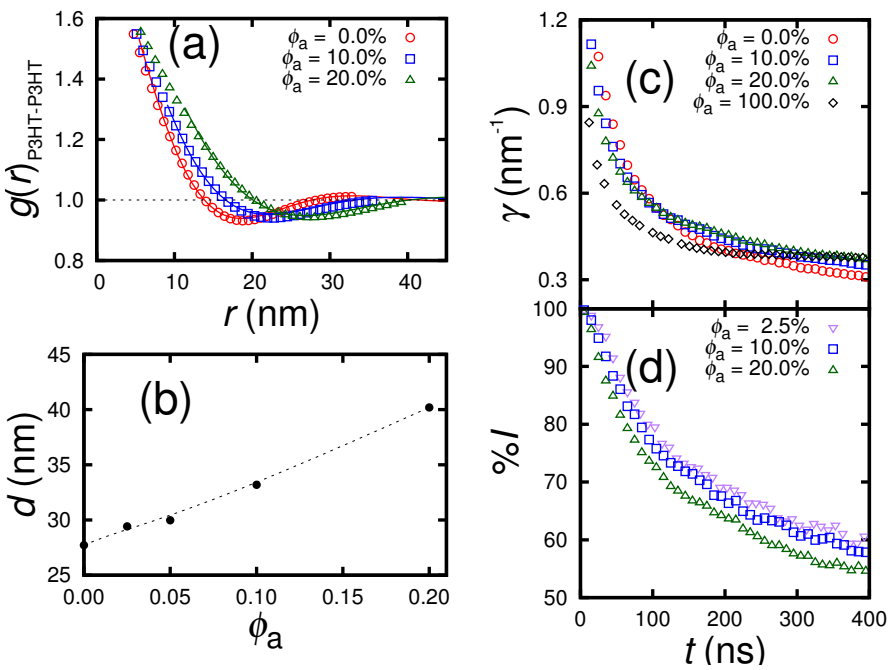

Figure 3: CGMD simulations results of bulk systems. (a) Radial distribution function of P3HT beads, $g(r)_{\mathrm{P3HT-P3HT}}$, at $t = 200$ ns of simulation time and different ϕ_a. The lines are fits using Eq.4 (b) Domain size, d, as a function of ϕ_a obtained using Eq.4 to fit spatial correlation functions shown in (a). (c) Evolution of the interfacial surface area to volume ratio, γ. (d) Percent of short P3HT chains that are in contact with long P3HT chains and PCBM domains, $\%I$.

Figure 3(c) shows results of calculations for γ, which adopts the method described in our earlier work.[25] In brief, γ is calculated by summing the total surface area of Voronoi polyhedra faces belonging to both P3HT and PCBM beads. Similar to the pattern of behavior captured in d, a monotonic increase in γ is observed as the relative amount of short-chains added, ϕ_a, increases. The observed trend of increasing γ as d increases seems counterintuitive—one might expect γ to decrease as d increases for systems with smooth interfaces and pure domains. However, the increase in γ as d increases distilled from simulation results indicates that the interface formed between PCBM and P3HT is not smooth and the P3HT and PCBM domains are not pure due to the partial miscibility of short P3HT chains. This miscibility

can be seen in Figure 2 by noticing that at domain interfaces, some of the short chains (blue beads) encroach into the PCBM domain (white areas). We note that while it appears that some of the red beads also cross the domain interfaces, this is an artifact resulting from slicing the simulation box, producing a 2D representation of the 3D morphology.

It is important to determine the location of the short chains relative to the more concentrated long chains to ascertain the extent of short-chain miscibility with PCBM. To do this, we calculated the percentage of short chains in the interface, $\%I$, (see Figure 3 (d)) which is an indicator of the amount of short chains straddling the interface. This calculation takes advantage of the ability of the simulation to track long and short chains, which allows the determination of the number of short-chains that are in contact with both PCBM beads that are not dissolved in the P3HT matrix and monomers belonging to long-chain P3HT, $m_{s,int}$, relative to the total number of short chains, m_s: $\%I = (m_{s,int}/m_s)100\%$. Figure 3(d) shows that $\%I$ decreases with respect to simulation time and the value of $\%I$ decreases as ϕ_a increases. It is noteworthy that more than half of the short-chains P3HT are at the interface: As the system evolves toward equilibrium, values of $\%I$ exceed 50% for all of the systems considered. This should not come as a surprise because the effective χ_{12} parameter for $N_s = 10$ is lower than that for $N_l = 100$ and the intermixing of PCBM and short chains favors an increase in entropy of the system. We note that even at t=400 ns, the value of %I has not reached equilibrium, however we expect the observed trends will not change.

To summarize the results on bulk systems, the addition of small amounts of short chains results in an increase in the electron donor domain size d and interfacial area-to-volume ratio γ in bulk systems constituted to mimic a BHJ thin film. The short chains are preferentially located at the P3HT/PCBM interface. We emphasize that these trends are valid because of the long simulation run-time of $t = 400$ ns, which is near equilibrium—where the values of γ, d and $\%I$ are changing slowly and are approaching their saturation values.[25] This simulation time is not to be confused with the experimental annealing time since the CGMD system, which employs a smooth force-field leading to lower potential energy barriers, converges

faster than experiments.

With these results in mind, we proceed with analyzing the simulation results for systems with bounding substrates. In Figure 4(a) we show the average vertical distribution (volume fraction) of PCBM as a function of z, $\phi_{\mathrm{PCBM}}(z)$, where z is the distance from the bounding substrate, which is modeled as silicon (see Figure S.1) for consistency with neutron reflectivity experiments. This calculation, which is done using radical Voronoi (or Laguerre) tessellation,[45] shows that in the middle portion of the film, the value of $\phi_{\mathrm{PCBM}}(z)$ fluctuates about the overall composition of the film. However, $\phi_{\mathrm{PCBM}}(z)$ is greater than the overall average composition of the film in the vicinity of both air and silicon substrate interfaces, which indicates that these regions are enriched with PCBM. (Although the silicon is established to have a 1 nm thick oxide layer thickness on it, we refer to it simply as "Silica".) The value of ϕ_{PCBM} near the silicon substrate for $\phi_a = 0.0\%$ peaks at 0.755, which agrees with the value used to parameterize the substrate-to-bead pair-wise interactions, described in the *Supporting Information*. However it is interesting to note that for $\phi_a = 10.0\%$, ϕ_{PCBM} near the silicon substrate peaks at 0.716, which represents a 5% decrease in PCBM enrichment relative to the situation where no low molecular weight additives are present.

Given that the presence of short chain additives affects the composition profile, we calculate the normalized change in the local composition of P3HT relative to the overall film composition, $\Delta\phi_{\mathrm{P3HT}}(z)/\phi_{\mathrm{P3HT}}$ in the film thickness dimension:

$$\frac{\Delta\phi_{\mathrm{P3HT}}(z)}{\phi_{\mathrm{P3HT}}} = \frac{\phi_{\mathrm{P3HT}}(z) - \phi_{\mathrm{P3HT}}}{\phi_{\mathrm{P3HT}}} = \frac{\phi_{\mathrm{P3HT}}(z)}{\phi_{\mathrm{P3HT}}} - 1 \tag{5}$$

Using this formalism, and because the simulations enable the short and long chains to be distinguished, it is possible to tease apart the overall composition profile (see Figure 4) to examine how the long and short chains distribute themselves in the BHJ thin film. As shown in Figure 4(b), which displays results for the system having $\phi_a = 10\%$, we observe that there is an enrichment of long chains at the silicon/film interface relative to the short chains. Self-consistent field theoretical (SCFT) calculations of dilute to moderately concentrated

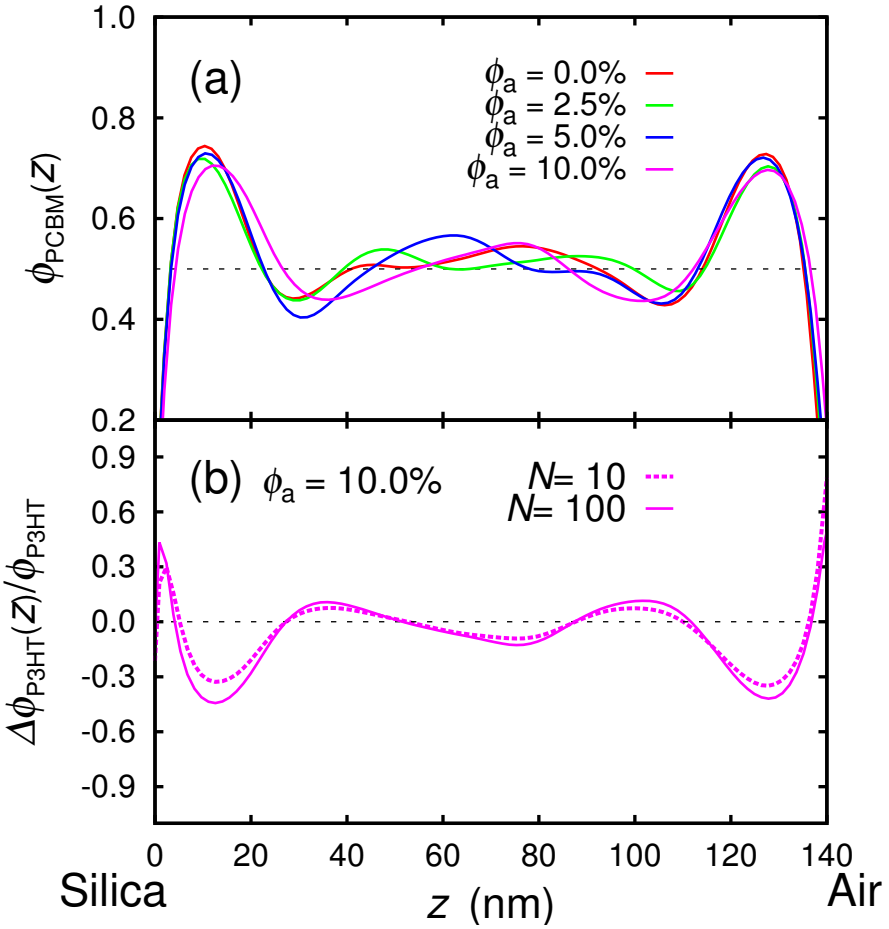

Figure 4: (a) Laterally averaged vertical distribution of the PCBM volume fraction, $\phi_{\mathrm{PCBM}}(z)$, at $t = 400$ ns and different ϕ_a computed using radical Voronoi (or Laguerre) tessellation. (b) Normalized change in vertical distribution of short and long P3HT polymers in the thickness dimension of the film, $\Delta\phi_{\mathrm{P3HT}}(z)/\phi_{\mathrm{P3HT}}$, at $t = 400$ ns for the system with $\phi_a = 10\%$.

polymers in contact with an adsorbing substrate supports this observation.[46] On the other hand, it is observed that the short chains are more abundant at the air/film interface. Since the air/film interface is athermal (non-adsorbing) in the simulations, the short chains are more easily accommodated in this region because their high number density of chain ends (relative to long chains) reduces the loss of translational entropy.

The locations of the PCBM domains across the depth of the BHJ can be obtained from images of the cross section of the final trajectory frame produced by the simulations. Figure 5 displays results for the $\phi_a = 10.0\%$ system, with a region cut-away to provide views in the three principal dimensions of the film. Figure 5(a), which shows the distribution of PCBM and 5(b), which shows long (red) and short (blue) P3HT chains, are complementary images of the same film. As with the bulk system, the film phase separates into PCBM-rich and P3HT-rich domains, with short (blue) chains intermingled in the PCBM domains due to their miscibility and ability to pack. Figure 5(c) shows slices (through the plane of the film) at different heights to highlight how the local concentration of PCBM fullerene changes in the thickness dimension of the film. These results clearly show the enrichment of PCBM both near the silicon ($z = 12$ nm, leftmost image) and near the air ($z = 115$ nm, rightmost image) interfaces. In total, the simulations reveal fine details of the segregation of short and long P3HT chains, thereby providing a clear and three dimensional representation of the BHJ morphology.

As noted earlier, the size of the system (simulation box) was chosen to allow comparisons to be made between the results from CGMD simulations and specular neutron reflectivity (NR) measurements. This need arises because in NR, while the short wavelength of neutrons allows nanoscale resolution of film composition (structure) in the film thickness dimension, this composition is laterally averaged over the film area illuminated by the neutron beam which is incident at shallow angles. In other words, the quantity generated from CGMD simulations that is used for comparison with specular NR data is the laterally averaged volume fraction in the z direction, which is shown in Figure 4(a).

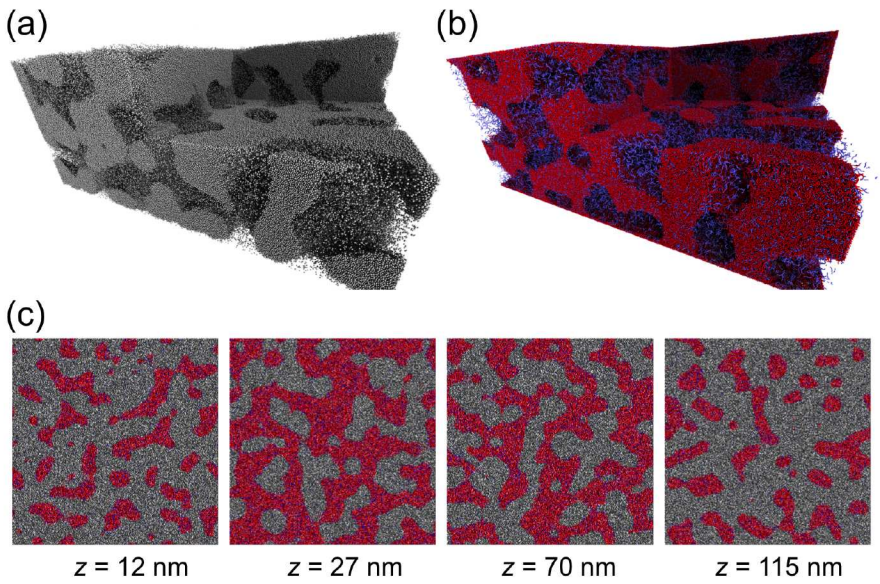

Figure 5: Snapshot of a cross section of the $\phi_a = 10.0\%$ system at $t = 400$ ns showing the PCBM (gray beads) domains, long P3HT chains (red beads) and short P3HT chains (blue beads). Only PCBM beads are shown on (a) and the complementary image on (b) shows the P3HT domains, which features short P3HT chains that are situated at P3HT/PCBM interfaces. The slices on (c) at different planes highlight the non-uniform distribution of the PCBM and P3HT domains in the direction perpendicular to the silicon substrate, which illustrates the enrichment of PCBM near the top ($z = 115$ nm) and bottom ($z = 12$ nm) interfaces.

We proceed to compare the CGMD results with NR measurements by first calculating the scattering length density (SLD) profile, or $\Sigma(z)$, from simulation results (see Figure S.3(b) in the *Supporting Information*). This profile can be calculated by using known SLD values, Σ, of the pure components which are Σ_{Si}, $\Sigma_{\mathrm{SiO_x}}$, Σ_{PCBM}, Σ_{P3HT} and Σ_{Air}, for silicon, silicon oxide, PCBM, P3HT and air, respectively. Because a physical substrate is not explicitly included in the SLD profile that can be obtained from simulations, we augment the SLD profile by adding a slab (bounding surface) consisting of pure silicon (thickness = 9 nm) having a thin $\mathrm{SiO_x}$ layer atop (thickness = 1 nm), which matches the samples used in NR experiments. We also truncated 4.5 nm of the P3HT/PCBM blend near the silicon substrate. This truncation is justified since the coarse-grained parameters of PCBM and P3HT are ambiguous in the vicinity of the silicon substrate because this region is at a different thermodynamic state point from the bulk (the coarse-grained model parameters are not transferable in this region). The truncation is in the region where the $\phi_{\mathrm{PCBM}}(z)$ is equal to the overall PCBM concentration and before the peak of $\phi_{\mathrm{PCBM}}(z)$, which occurs at $z \approx 10$ nm. The calculation of the SLD profile of the P3HT/PCBM blend (the region in between the silicon substrate and air) uses Eq.6[47] where the $\phi_{\mathrm{PCBM}}(z)$ values used in the calculation are shown in Figure S.3(a) in the *Supporting Information*.

$$\Sigma(z) = \phi_{\mathrm{PCBM}}(z)(\Sigma_{\mathrm{PCBM}} - \Sigma_{\mathrm{P3HT}}) + \Sigma_{\mathrm{P3HT}} \tag{6}$$

This approach was used to determine $\Sigma(z)$ for systems with $\phi_a = 0.0\%$ and with $\phi_a = 10.0\%$ at $t = 400$ ns, which represents systems after thermal annealing, and for the system with $\phi_a = 0.0\%$ at $t = 10$ ns, which represents a system without additive at the onset of thermal annealing. The SLD profiles for these systems (with the silicon substrate in place) are shown in Figure S.3(b). The trajectory at $t = 10$ ns corresponds to a system where the BHJ morphology is changing rapidly during annealing. As is evident from the results shown in Figure 3 and our previous work,[25] $t = 400$ ns represents a system where the morphology is almost constant, corresponding to annealed BHJ films.

The reflectivity, R, was calculated analytically using the Parratt formalism, where the reflectivity of the P3HT/PCBM blend is a function of the optical transform matrix M.[48] The $\phi_{\mathrm{PCBM}}(z)$ data obtained in Figure 4(a) and the bin size Δ_{S} of the data were used for the values for $\Sigma(z)_i$ and thickness of the slice for the transfer matrix M_i calculation for each i of the set of uniform layers. The reflectivity profiles obtained using CGMD SLD profiles are shown in Figure 6(a), which presents the data as RQ^4 *versus* Q, where Q is the wavevector transfer ($4\pi\sin(\theta)/\lambda$). Here again, albeit through a different representation of the physical situation, it is observed that the presence of a short-chain additive impacts the morphology of the BHJ thin film. It is also worth noting that while simulations can be used to deduce fine details of how long and short chains and PCBM arrange themselves in the BHJ film, in a scattering experiment, the structure at different length scales manifests in the scattered intensity at all Q values.

To enable comparison with experiments, the calculated reflectivity is convoluted point-by-point with a Gaussian function representing the instrument resolution ($\delta Q/Q = 0.03$). Recall that the Q spacing between the fringes in the reflectivity curves for these simple films is proportional to the inverse of the total film thickness: $\Delta Q \sim 2\pi/d_{\mathrm{tot}}$. Segregation of different scattering density material to film surface and substrate manifests as damping and modulation of these total-film-thickness interference fringes and the envelope on which they ride.[49,50] In the simulation results, shown in Figure 6(a), we found that at low Q, the intensities of the fringes for the system with short P3HT chains (blue) are generally lower than that of the system with long P3HT chains only (green). The experimental data (Figure 6(b)) are less straightforward to interpret. Most obvious and least important, the total thickness of the control and additive films was not identical, so the fringes for the thicker control film are more closely spaced. More importantly, the fringes of the additive-containing film are not as sharp as those of the control, broadly indicative less well-defined surface and substrate interfaces. It is not possible to make a quantitative comparison between the two sets of results because the experiments, as mentioned previously, not only have layer

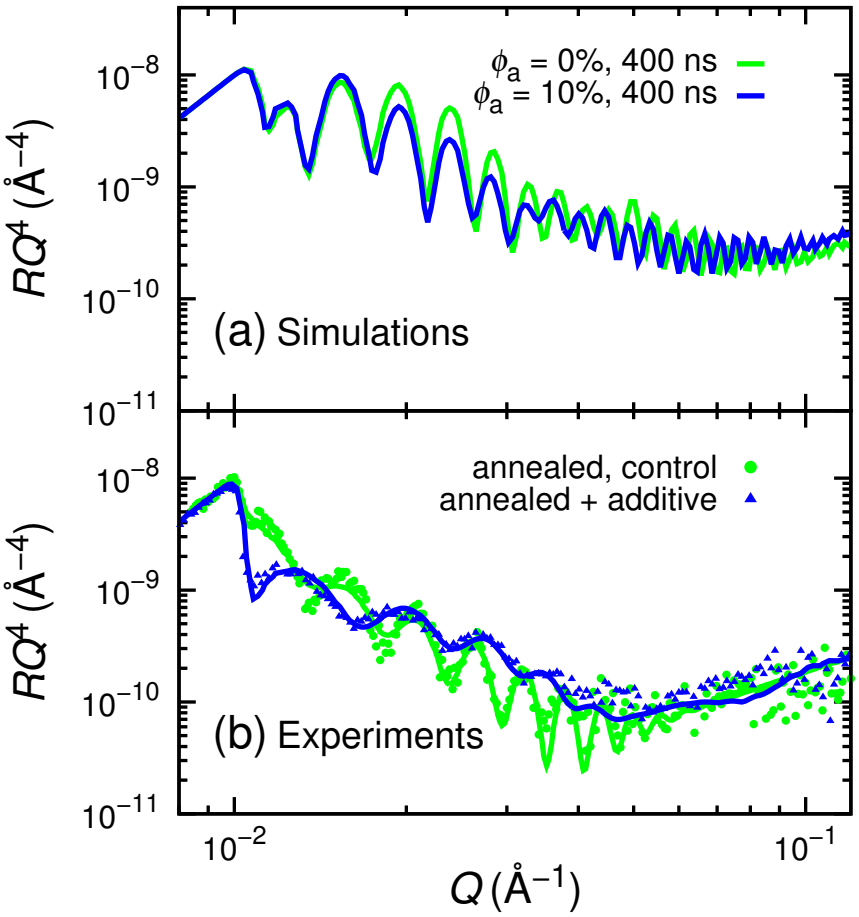

Figure 6: Comparison of the neutron reflectivity, R represented as RQ^4 *versus* Q, where Q is the wavevector transfer, determined from simulations (a) and experiments (b) The lines in (b) are fits of the neutron reflectivity data.

thickness different than those of the simulations, but also have a different blend composition. Difficulties in attaining the same film thickness likely arise due to different surface energies of short and long P3HT, and solubility of short and long P3HT with PCBM and casting solvent. Also, it has previously been reported that similar P3HT/PCBM films processed using spin-coating feature voids that account for as much as 40% of the volume fraction at the air interface.[51] These voids are not included in the simulations, where uniform thickness across the film is imposed.

Nevertheless, experimental data are well described by a three-layer model having zones of enrichment of PCBM near the air and silicon interfaces, which strongly correlate with the laterally-averaged composition profiles produced by petascale CGMD simulation. To further analyze the neutron reflectometry experiments, the data presented in Figure 6(b) were fit and the resulting scattering length density profiles for the system with and without additives after the annealing procedure are shown in Figure S.4(b) in the *Supporting Information*. These are transformed into the local PCBM concentration, $\phi_{\mathrm{PCBM}}(z)$, using Eq.6 considering only the region where P3HT and PCBM are found (excluding Si/SiOx layers) and presented in Figure S.4(a) and Table S.3 in the *Supporting Information*. It can be seen in Figure S.4(a) that the thickness of the film and the total PCBM concentration for the systems with and without additives are not identical due to difficulties in casting a film of the same composition and thickness.

To gain insight on the relative decrease of the PCBM composition enhancement near the substrate and air interfaces, we normalized the concentration of PCBM relative to its bulk concentration (concentration at the middle of the film), similar to the procedure that we employed in presenting Figure 4(b) using Eq.5. It can be seen in Figure 7 that in the system without the low molecular weight additive, the concentration of PCBM at the interfaces are 60% higher than the composition at the middle of the film. However, for the system with the low molecular weight additive, the enrichment is only 10% greater. Also, the relative thicknesses of the PCBM-rich regions near the SiO_x and air interfaces are thicker

in the control system. Thus, similar to the results of the CGMD simulation, the neutron reflectometry experiments show that the system with low molecular weight P3HT additive has a more uniform PCBM concentration in the film thickness dimension.

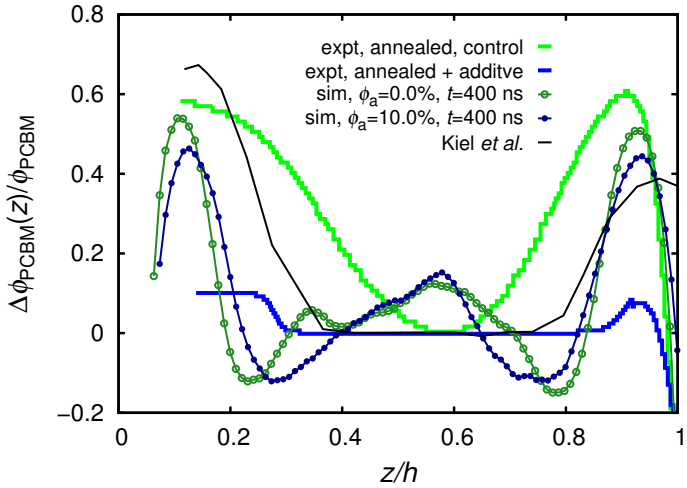

Figure 7: Normalized change in vertical distribution of PCBM in the thickness dimension of the film , $\Delta\phi_{\mathrm{PCBM}}(z)/\phi_{\mathrm{PCBM}}$, where h denotes the thickness of the layer composed of Si, SiOx, P3HT and PCBM for both CGMD and NR results. The NR data by Kiel *et al.*[7] is included for comparison.

Atomistic simulations of chain distribution and orientation across donor/acceptor interfaces

Using surface photovoltage spectroscopy experiments, Osterloh *et al.*[42] showed that charge transfer states generated in crystalline P3HT regions of the P3HT/PCBM BHJ diffuse to and then separate at the P3HT/PCBM interface through a band gap excitation mechanism, forming free and mobile charges. From quantum chemical and molecular dynamics simulations of semiconducting π-conjugated organic materials, it is known that the efficiency of the charge transfer is extremely sensitive to molecular packing and relative orientations of the conjugated rings.[52,53] Motivated by this understanding and given that CGMD simulations show that short chain additives populate donor/acceptor interfaces, we perform molecular

dynamics simulation at the atomistic level to gain insight into how thienyl rings belonging to short chains organize and interact at donor/acceptor interfaces.

We choose the initial configuration of our simulation based on our results from coarse-grained MD simulations. We assume that the BHJ has a phase separated morphology with pure crystallized components as the core of each domain. These domains are surrounded by a broad, amorphous region where the small molecules or oligomers are situated. This assumption is justified based on a variety of results and observations. Specifically, this morphological arrangement agrees with the experimentally observed "rivers and streams" model[54] consisting of pure P3HT crystals and pure PCBM phases separated by a miscible phase of amorphous P3HT and PCBM and is also consistent with the P3HT/PCBM morphology proposed by Wu *et al.*,[35] who used simultaneous grazing-incidence small-/wide-angle X-ray scattering (GISAXS/GIWAXS) experiments to show that the BHJ consists of intercalated PCBM aggregates and P3HT crystallite blocks that are immersed in a matrix of amorphous P3HT chains and dispersed PCBM molecules. The model employed in our simulations is also buttressed by work from Russell *et al.*,[30] who showed that low molecular weight P3HT chains are more miscible with PCBM, and by the understanding that crystallization of P3HT is a one-dimensional heterogeneous nucleation with linear growth kinetics[55] that is in competition with PCBM aggregation.[35] Together these suggest the formation of an amorphous interface[56] where the low molecular weight P3HT chains can be found. We simplify our model by assuming that the interface is composed of only PCBM and amorphous P3HT oligomers and the crystalline cores do not interact with the interface. Hence, the model of the amorphous layer, composed of the interface and bulk regions but without domains of crystalline PCBM and P3HT, can be modeled as two periodic slabs of P3HT and PCBM that are in intimate contact, as shown in Figure 8. This simulation strategy provides a means to quantify the interfacial layer thickness and the orientation of the thiophene rings relative to the interfacial plane where the slabs of amorphous P3HT and PCBM meet.

The force field used for the atomistic MD simulation is the Generalized Amber Force

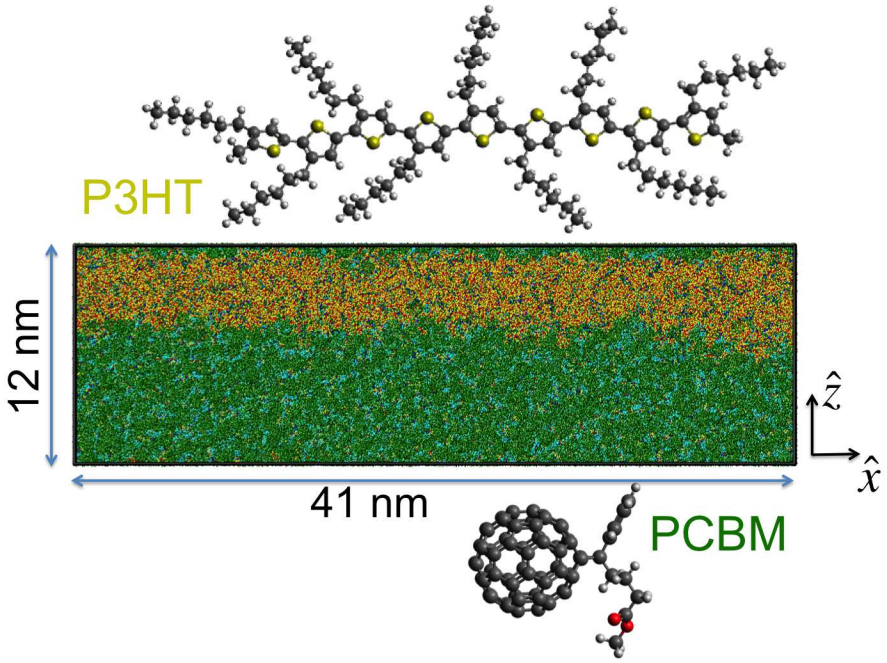

Figure 8: Snapshot of the simulation box used for atomistic MD simulations of the interface between P3HT oligomers (yellowish region) and PCBM (green region).

Field (GAFF)[57] which is classified as a "Class I" model that includes descriptions of bonded (*e.g.*, bonds, angles and dihedrals) and non-bonded (*e.g.*, van der Waals and Coulomb) interactions. (More details of the atomistic MD simulations are presented in the *Supporting Information*). To and Adams[58] showed that the functionals in a "Class I" force-field are adequate to describe and validate the structure of P3HT and PCBM. However, unlike the model used by To and Adams, the force field used here was not validated for the crystal structure and melting point temperatures of P3HT and PCBM. We argue that we do not need to model the crystal structure formation because we are interested in the amorphous P3HT/PCBM interface, where our CGMD simulations show the short chains residing. It is known that films comprising P3HT of broader dispersity are known to be less crystalline than those consisting of P3HTs with narrow molar mass distribution;[59] hence we posit that short P3HT chains have lower probability of integrating into P3HT crystals based on entropic (higher system entropy if it remains disordered and mixed with PCBM) and steric arguments (more difficult to fit into a crystal that is made from long P3HT chains). Although it is also

possible that the short chains serve as nucleation sites, we did not take this into consideration.

The simulations were performed in an isobaric-isothermal (NPT) ensemble at temperatures equal to 300 K and 423 K and atmospheric pressure using LAMMPS with GPU acceleration in OLCF's Titan. The simulation box was setup at a P3HT:PCBM weight ratio of 1:4 with P3HT oligomers which have 3, 6 and 9 repeat units. The use of a high PCBM loading ensures that a PCBM domain is maintained, which allows an interfacial plane that is parallel to the xy-plane to be easily identified. This simulation, which consists of ∼1.8 million atoms, was run for 64 ns because it was found that the total energy of the simulation system saturates at ∼40 ns. The final 4 ns were used for data analysis.

Figure 9(a) shows the density profile in the dimension of the simulation box orthogonal to the interface, which was calculated by averaging an ensemble of 400 trajectory frames in the final 4 ns of the simulations. To generate the density profile of P3HT oligomers, shown for the case of $N = 6$ in Figure 9(b), the corresponding P3HT density profile across the two interfaces (red-circles in Figure 9(a)) was averaged. Here we display the resulting oligomer density profile by shifting the data such that $z = 0$ is at the middle of the interface (Fig.9(b)). In Figure 9(c), the density profile in Figure 9(b) was scaled relative to the bulk density (average density farthest from the two interfaces, or the density at the center of the P3HT slab, ρ_b), as described by the equation,[60]

$$\Psi(z) = \frac{2}{\rho_b}\left(\rho(z) - \frac{\rho_b}{2}\right). \tag{7}$$

$\Psi(z)$ can be fit with a hyperbolic function,[60,61]

$$\Psi(z) = \tanh\left(\frac{2z}{w}\right) \tag{8}$$

and the variance in the derivative of the scaled profile, Δ^2, can be calculated analytically as the (normalized) second moment of the derivative of the segment density distribution:

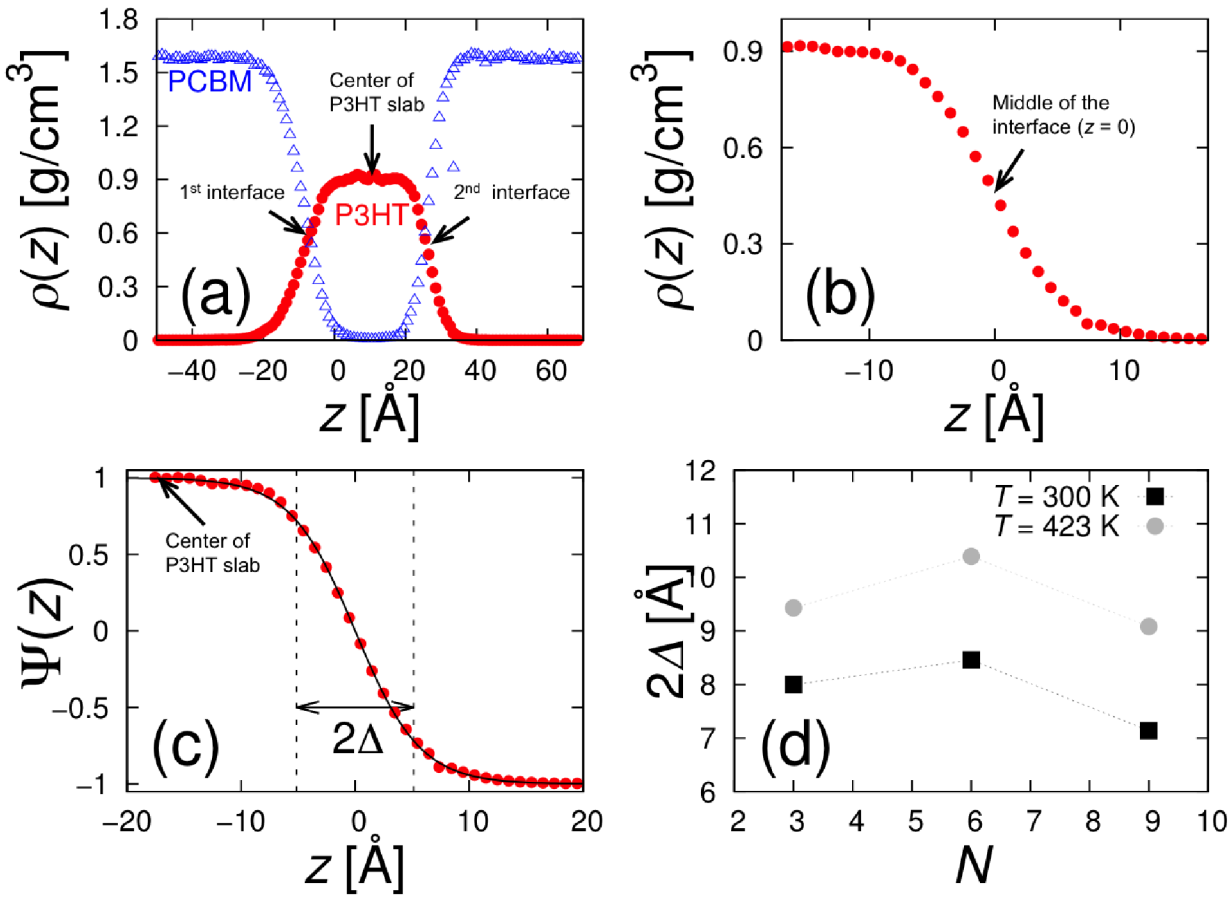

Figure 9: Results of the atomistic MD simulations showing (a) the density profile $\rho(z)$ for a system where the P3HT oligomers are of size $N = 6$. The total P3HT:PCBM weight ratio in the system is 1:4. (b) Average density profile of P3HT, (c) scaled density profile, $\Psi(z)$, and interfacial thickness, 2Δ for the system described by (a), (d) Interfacial thickness, 2Δ, as a function of degree-of-polymerization, N, at temperatures of 300 K and 423 K (d). The dashed lines in (d) are merely intended to guide the eye.

$$\Delta^2 = \frac{\int_{-\infty}^{\infty} z^2 \Psi'(z) dz}{\int_{-\infty}^{\infty} \Psi'(z) dz} = \frac{\pi^2 w^2}{48} \tag{9}$$

The result of these manipulations allows interfacial thickness, $2\Delta = \pi w/2\sqrt{3}$, to be quantitatively determined.

The results, depicted in Figure 9(d), show that the interfacial width 2Δ increases with increasing temperature, as expected; however, a non-monotonic dependence of 2Δ with respect to the number of repeat units in an oligomer, N, is observed. It is expected that smaller oligomers would lead to a more diffuse interface,[62,63] but as seen in Figure 9(d), the largest interfacial width is observed for $N = 6$. We speculate that this behavior is related to how the oligomers pack in relation to PCBM and to other P3HT oligomers, since we also observed non-monotonic behavior in ρ_b (density at the center of the P3HT slab obtained from the simulations) as a function of N. (Results not shown).

We investigate the reason behind the observed non-monotonic behavior of the interfacial thickness by inspecting the conformation of the P3HT oligomers, which provides insight into the organization of chains across domain interfaces. This was done by computing the orientation of the thiophene rings relative to the interface, with the angle θ defined as the angle between the vectors normal to the interfacial plane and normal to the face of each thiophene ring. Figure 10(a) shows the orientation of the thiohene rings, represented by $\langle \cos^2(\theta) \rangle$ as a function of the distance between its center-of-mass across the film in the z direction. A value of $\langle \cos^2(\theta) \rangle = 1$ describes the situation where the thiophene rings are parallel to the interface, which is defined as the xy-plane in the system geometry. At the center of the P3HT slab $\langle \cos^2(\theta) \rangle = 1/3$, which indicates an isotropic orientation. Near the middle of the interface ($z \approx 0$ Å), $\langle \cos^2(\theta) \rangle$ is higher than 1/3, indicating that the parallel configuration is favored. It is also observed that the peak value of $\langle \cos^2(\theta) \rangle$ increases as N increases. The average orientation of the thiophene rings near the middle of the interface are face-on with respect to the PCBM molecules. (See Figure 10(c).) As a point of reference, molecular dynamics simulations[58] and density functional theory[64,65] calculations showed that

the face-on P3HT configuration was found to be the most energetically favored configuration.

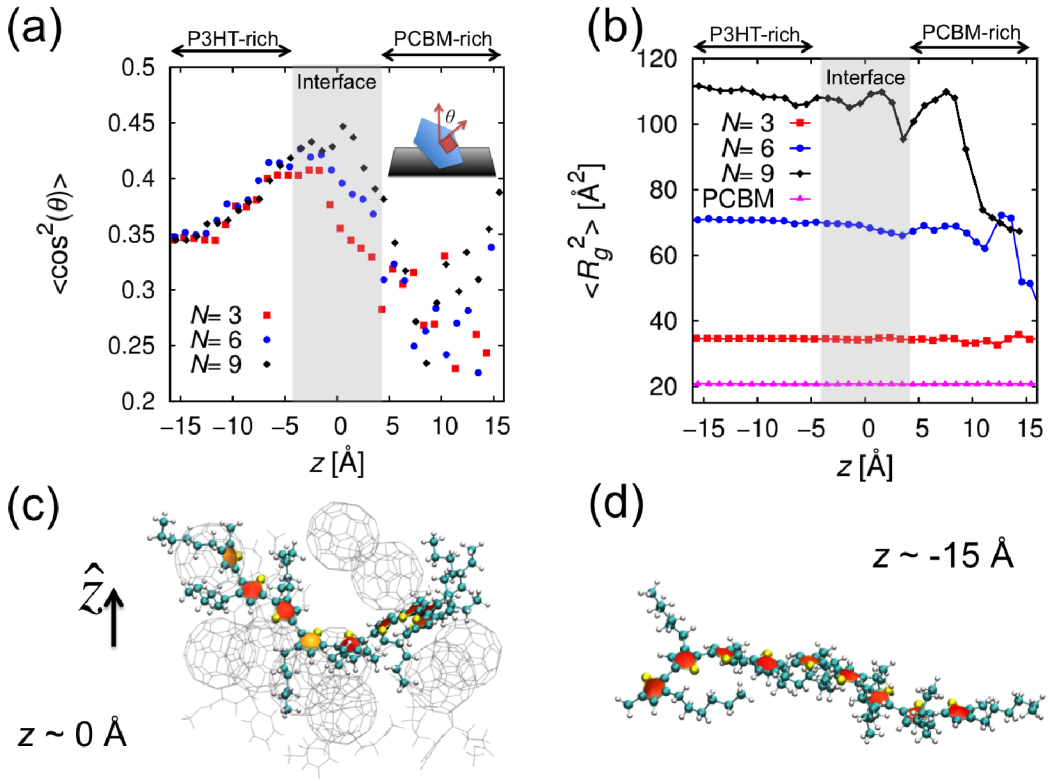

Figure 10: (a) Orientation of thiophene rings represented by $\langle \cos^2(\theta) \rangle$ across the film taken as the interval from $z = -15$ Å to $z = 15$ Å, where $z = 0$ Å is the middle of the interface and $z = -15$ Å is near the center of the P3HT slab. (Refer to Figure 8(c).) The shaded region is the interface. Left of the interface is the P3HT-rich region while the PCBM-rich region is to the right. θ is the angle between the vector normal to the interfacial plane (z-axis) and normal to the face of the thiophene ring, as shown in the inset. (b) Mean-square radius of gyration, $\langle R_g^2 \rangle$, as a function of the z-component center-of-mass of P3HT and PCBM molecules. Typical conformation of oligomers with $N = 9$ at the (c) middle of the interface with its PCBM neighbors and at the (d) center of the P3HT slab.

Another way to capture differences in sizes and conformations of P3HT oligomers of different size across the film is by examining the mean-square radius of gyration, $\langle R_g^2 \rangle$, which is displayed in Figure 10(b) for the three oligomers and for PCBM. In calculating $\langle R_g^2 \rangle$, we assigned the van der Waals volume as weights for the normalization value such that

$$\left\langle R_g^2 \right\rangle = \frac{1}{V_w} \left\langle \sum_{i=1}^{N_{atom}} \left(\frac{4}{3} \pi r_{w,i}^3 \right) (\vec{R}_i - \vec{R}_{cm})^2 \right\rangle \tag{10}$$

Here V_w is the van der Waals volume of the molecule, r_w is van der Waals radius of an atom in the molecule, and $\vec{R}_{cm}$ is the center-of-mass of the molecule. The coarse-grained description of P3HT chains in the CGMD simulations described in the previous section estimates that a persistent segment is comprised of $N = 10$ repeat units. Therefore, we expect that the conformations of the oligomers in the atomistic MD simulations that are situated far from the middle of the interface and distant from the effects of PCBM are rod-like. This was confirmed by probing the conformations of oligomers in the atomistic MD simulation that are in the middle region of the amorphous P3HT slab. As observed from the structural model shown in Figure 10(d), the backbone of these chains in the middle region of the P3HT slab is persistent (rod-like) and the thiophene rings are oriented in such a way that they are almost coplanar. A decrease in the value of $\left\langle R_g^2 \right\rangle$ would indicate a distortion or bending of the rod. The oligomers having $N = 6$ and 9 repeat units that are near the interface and in contact with PCBM are distorted and conform to the surface of neighboring PCBM molecules. This is reflected by their lower $\left\langle R_g^2 \right\rangle$ values and exemplified in the optimized structural model shown in Figure 10(c). In contrast to the behaviors of the $N = 6$ and $N = 9$ systems, the $\left\langle R_g^2 \right\rangle$ of $N = 3$ oligomers hardly changes across the film indicating that these small oligomers are undeformed. The $N = 3$ molecules are almost of the same size as the PCBM molecules and, therefore, can organize more easily around a PCBM molecule without distorting their configuration. This faciliates packing of P3HT oligomers, resulting in a less diffuse interface in comparison to the system with $N = 6$ oligomers. Thus, there is a difference in the packing process between $N = 3$ and $N = 6$ oligomers: the former represents a case where packing is of similarly configured molecules, while the latter is a situation where packing accommodates an ensemble of variably deformed molecules. These differences in how the oligomeric P3HTs pack with PCBM molecules manifests in a lower 2Δ for $N = 3$ than for $N = 6$, which seems to be a reasonable explanation for the non-monotonic behavior of the interfacial thickness,

2Δ, as a function of N. As noted at the outset of this section, in photovoltaic systems changes in orientation matter, as relative orientation and packing of chains impact charge transfer processes.

Electronic structure across the electron donor and acceptor interface

Sharber *et al.*[66] demonstrated that the open-circuit voltage of BHJ devices using PCBM as acceptor is determined by the lowest unoccupied molecular orbital (LUMO) and highest occupied molecular orbital (HOMO) levels of PCBM and the donor, respectively. We expect that the LUMO level of PCBM to remain constant across the interface because of its spherical structure. However, this might not be the case for semiflexible P3HT chains because the thiophene rings impart a certain degree of rigidity and also because orientation varies across the interface. To examine this issue, which originates in the nanoscale orientation and packing arrangement of the repeat units, we evaluated the HOMO and LUMO levels of the P3HT oligomer to determine whether conformational changes across the interface manifest as changes in electronic structure. Using the last frame of the atomistic molecular dynamics simulation run, we randomly chose sample configurations (approximately 130 configurations) of P3HT oligomers spanning 27 Å in the interface region (approximately 5 configurations per Å). We performed single point DFT calculations employing a B3LYP/6-31G* basis set using NWChem.[67] In DFT, the electron affinity (EA) and ionization potential (IP) are obtained from the LUMO and the HOMO orbital energies, respectively. Hence, we refer to EA as $\mathrm{EA_{LUMO}}$ and IP as $\mathrm{IP_{HOMO}}$. The calculations were done without geometry optimization in order to examine changes in the LUMO and HOMO energy levels brought about by the change in configuration of the polymer chain as a function of location across the interface. This approach preserves the effect of the chemical environment on the conformation of the oligomer. The indexing across the interface is based on the center-of-mass location of the oligomer. Although there are significant differences in the orientation of the thiophene rings

as a function of z as shown in Figure 10, in Figure 11 we did not observe any significant differences in the IP_{HOMO} (blue filled squares) and EA_{LUMO} (blue open squares) energy levels across the interface (on a per molecule basis) for the systems with $N = 6$. (Similar results are seen in systems with $N = 3$ and $N = 9$.)

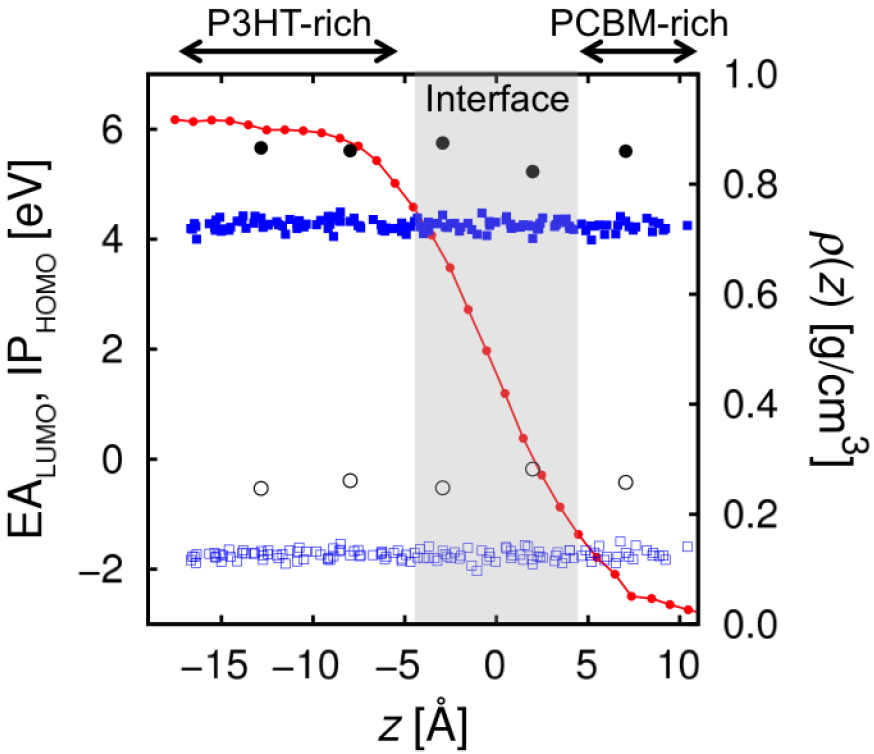

Figure 11: EA_{LUMO} (open symbols) and IP_{HOMO} (filled symbols) energy levels across the interfacial layer calculated by single point DFT calculations (blue squares) and coupled cluster (CCSD) calculations (black circles) based on the geometries of $N = 6$ P3HT oligomers. The density profile of P3HT (red circles) is superimposed to indicate the position of the interface and locations of the P3HT and PCBM domains.

To verify the robustness of the observation that LUMO and HOMO values of P3HT oligomers do not change appreciably across the interface, we repeated the DFT calculations using larger spherical Gaussian basis sets (6-31++G** and 6-311++G**).[68] We selected five representative molecules from the $N = 3$ and $N = 6$ systems that sample the different regions across the donor/acceptor interface and compared these results to the EA_{LUMO} and IP_{HOMO} values calculated from the larger set of ∼130 structures sampled to create the data presented

in Figure 11. As shown in Table S.5 (in the *Supporting Information*) the DFT calculations show that the absolute value of both LUMO and HOMO increase with an increase in size of the basis set used, however, the difference between the LUMO and HOMO values for the five samples (at constant basis set) is not significant. Furthermore, we calculated the IP and EA using the more accurate but computationally expensive IP and EA extensions of the equation-of-motion coupled cluster (IP/EA-EOM-CCSD)[69–72] calculation method (using 6-31+G basis set for $N = 3$ and 6-31G basis set for $N = 6$), where the theoretical basis of this method is briefly described in the *Supporting Information*. The IP/EA-EOM-CCSD results, for $N = 3$ and $N = 6$ (shown in Table S.6 in the *Supporting Information*) demonstrates that the IP and EA values across the slab are not significantly different. To illustrate this point, we include in Figure 11 the IP (black filled circles) and EA (black open circles) for $N = 6$ obtained from IP/EA-EOM-CCSD. We recognize that accurate determination of electron affinities requires larger basis sets (triple zeta or TZ quality),[73–75] which would take us beyond the scope of this manuscript; but we expect similar results using large TZ basis sets.

That the LUMO and HOMO values of P3HT oligomers calculated using DFT and IP/EA-EOM-CCSD do not change appreciably across the interface suggest that the effect of orientation of thiophene rings on charge transfer is likely due to an inter-molecular and cooperative effect, instead of simply being based on the geometry of individual molecules. A similar coupling effect was seen by Troisi *et al.*,[76] Marchiori and Keohler[65] and Li *et al.*[64] in their studies of how packing of the small molecules and PCBM fullerenes affects charge transfer states. Unfortunately, it is challenging to account for inter-molecular coupling in DFT calculations because of the large system sizes involved in these calculations. Finally, it is relevant to note that this effect we see in systems containing small oligomers might not be the case for long polymer chains, where conformational changes could impact HOMO and LUMO levels.

Conclusions

The suite of studies that probe different length scales provide considerable insight into how small molecule oligomers influence the BHJ morphology, modify donor/acceptor interfaces, and affect electronic structure at those interfaces. These insights provide important context that will aid efforts to optimize morphology of BHJ systems and make connections with device performance characteristics. Results demonstrate that short P3HT chains reside at the donor-acceptor interface, modulating the BHJ morphology by swelling the P3HT domain. As the concentration of short chains increases, they mix into the PCBM domains, leading to larger donor domain sizes and higher interfacial surface area-to-volume ratios. In the presence of confining substrates, vertical phase segregation of PCBM is observed both near the silicon wafer substrate as well as the air interface. The presence of short chains in the thin film decreases the extent of vertical phase separation, which is qualitatively in agreement with neutron reflectometry measurements. Results from the atomistic MD simulations demonstrate that PCBM/P3HT interfacial width is a non-monotonic function with respect to oligomer size and thiophene rings at the interface favors orientation that is parallel to the PCBM domain. DFT calculations of P3HT across the interface show no appreciable change in the LUMO and HOMO energy levels of individual oligomers, suggesting that the effect of the orientation of the thiophene rings on the charge transfer across the interface is likely an inter-molecular and cooperative effect, rather than being due to the conformations of individual molecules.

While results are specific to P3HT/PCBM system, the methodologies used should be applicable to other conjugated polymer donor and fullerene acceptor systems. With petascale computing, we were able to perform large multiscale simulations that do not suffer from non-convergence, finite size effects and inadequate sampling statistics. These features, along with the ability to make comparisons with neutron scattering experiments and build in mesoscale effects such as polymer crystallization, represent a powerful and useful paradigm for accelerating the development of soft-matter based systems of OPV.

Methods

P3HT synthesis

Highly regioregular, low molecular weight P3HT with high H/Br end group content were synthesized *via* the Grignard metathesis (GRIM) polymerization method described by Loewe *et al.*[77] with slight modifications described our recent works.[14,78] In brief, the GRIM polymerization was quenched with HCl followed by sequential soxhlet extractions in methanol, acetone, and chloroform. Dibromo-3-hexylthiophene monomer was obtained from Puyang Huicheng Chemical Company and all other materials and solvents were obtained from Sigma Aldrich. Polymer molecular weight was determined using an EcoSec 1500 GPC with HPLC grade THF as the mobile phase.[14,78] End group distribution (> 95% H/Br end groups) was verified using matrix assisted laser desorption ionization time-of-flight mass spectrometry, as described by Kochemba *et al.*[79,80]

BHJ film casting

Solutions of PCBM and 30 kDa P3HT, either with a 5.6 kDa (determined by SEC) P3HT low molecular weight additive or without, were prepared using dichlorobenzene and a total composition of 0.7:1 P3HT:PCBM by weight. Solutions were stirred for 24 hrs. at 40 °C before deposition. Thin films that mimic BHJ architectures were deposited onto 5 mm thick, 50 mm diameter silicon substrates used for neutron reflectivity measurements *via* a two-stage spin-coating process that consisted of spinning at 400 rpm for 180 sec. followed by spinning for 20 sec. at 1400 rpm. Each sample was then immediately placed in a vacuum oven at room temperature for 10 min. to remove any residual solvent. After each as-cast measurement, samples underwent thermal annealing under vacuum at 150 °C for 15 min.

Neutron reflectivity measurements

Neutron reflectivity measurements were performed at the Spallation Neutron Source Liquids Reflectometer (SNS-LR) at ORNL. The reflectivity data were collected using a sequence of 3.25-Å-wide continuous wavelength bands (selected from 2.63 Å$< \lambda <$ 16.63 Å) and incident angles (ranging from $0.60° < \theta < 2.71°$). These selections translate to a momentum wavevector transfer, $Q = (4\pi \sin(\theta/\lambda))$, range of 0.008 Å$^{-1} < Q <$ 0.22 Å^{-1}. Reflectivity curves were assembled by combining seven different wavelength and angle data sets together, maintaining a constant sample illumination footprint and relative instrumental resolution of $\delta Q/Q = 0.03$ by varying the incident-beam apertures. The absence of off-specularly reflected neutrons was confirmed by inspection of the detector images from each sample measurement. An example of these scans featuring the critical edge ($q = 0.01$ Å^{-1}) is shown in Figure S.5 in the *Supporting Information*.

Supporting Information Available

Details of coarse-grained molecular dynamics simulations, atomistic molecular dynamics simulations, DFT, coupled cluster method, χ_{12} parameter (based on contact angles) calculations are presented. This material is available free of charge *via* the Internet at `http://pubs.acs.org`.

Acknowledgement

We thank C. Rycroft for assistance with Radical Voronoi analysis using MPI and Voro++, A.V. Dobrynin for assistance with the development of the substrate–BHJ interactions, T.D. Nguyen and W. M. Brown for assistance with LAMMPS MD code, and M. Chen for assistance with NWChem code. This research used resources of the Oak Ridge Leadership Computing Facility (OLCF) at the Oak Ridge National Laboratory (ORNL), which is supported by the Office of Science of the U.S. Department of Energy (DoE) under Contract No.

DE-AC05-00OR22725. This research was conducted in part at the Center for Nanophase Materials Sciences (CNMS) and at the Spallation Neutron Source (SNS), which are sponsored at ORNL by the Scientific User Facilities Division, Office of Basic Energy Sciences (BES), U.S. DoE. Experimental work of Z.S. and S.M.K. II was sponsored by National Science Foundation under award No. EPS 1004083. M.G. and J. -M. Y. C. acknowledge the Center for Accelerated Materials Modeling (CAMM), which is funded by the U.S. DoE, BES, Materials Science and Engineering Division (MSED). The computational work conducted by K.B.-N. and W.A.S. is supported by the U.S. DoE under EPSCoR Grant No. DE-SC0012432 with additional support from the Louisiana Board of Regents.

References

1. Collins, B. A.; Tumbleston, J. R.; Ade, H. Miscibility, Crystallinity, and Phase Development in P3HT/PCBM Solar Cells: Toward an Enlightened Understanding of Device Morphology and Stability. *J. Phys. Chem. Lett.* **2011**, *2*, 3135–3145.

2. Ruderer, M. A.; Müller-Buschbaum, P. Morphology of Polymer-Based Bulk Heterojunction Films for Organic Photovoltaics. *Soft Matter* **2011**, *7*, 5482–5493.

3. Liu, F.; Gu, Y.; Jung, J. W.; Jo, W. H.; Russell, T. P. On the Morphology of Polymer-Based Photovoltaics. *J. Polym. Sci., Part B: Polym. Phys.* **2012**, *50*, 1018–1044.

4. Sumpter, B. G.; Meunier, V. Can Computational Approaches Aid in Untangling the Inherent Complexity of Practical Organic Photovoltaic Systems? *J. Polym. Sci., Part B: Polym. Phys.* **2012**, *50*, 1071–1089.

5. Dou, L.; You, J.; Hong, Z.; Xu, Z.; Li, G.; Street, R. A.; Yang, Y. 25th Anniversary Article: A Decade of Organic/Polymeric Photovoltaic Research. *Adv. Mater.* **2013**, *25*, 6642–6671.

6. Kim, Y.; Choulis, S. A.; Nelson, J.; Bradley, D. D. C.; Cook, S.; Durrant, J. R. Composition and Annealing Effects in Polythiophene/Fullerene Solar Cells. *J. Mater. Sci.* **2005**, *40*, 1371–1376.

7. Kiel, J. W.; Kirby, B. J.; Majkrzak, C. F.; Maranville, B. B.; Mackay, M. E. Nanoparticle Concentration Profile in Polymer-Based Solar Cells. *Soft Matter* **2010**, *6*, 641–646.

8. Parnell, A. J.; Dunbar, A. D. F.; Pearson, A. J.; Staniec, P. A.; Dennison, A. J. C.; Hamamatsu, H.; Skoda, M. W. A.; Lidzey, D. G.; Jones, R. A. L. Depletion of PCBM at the Cathode Interface in P3HT/PCBM Thin Films as Quantified *via* Neutron Reflectivity Measurements. *Adv. Mater.* **2010**, *22*, 2444–2447.

9. Germack, D. S.; Chan, C. K.; Hamadani, B. H.; Richter, L. J.; Fischer, D. A.; Gundlach, D. J.; DeLongchamp, D. M. Substrate-Dependent Interface Composition and Charge Transport in Films for Organic Photovoltaics. *Appl. Phys. Lett.* **2009**, *94*, 233303.

10. Germack, D. S.; Chan, C. K.; Kline, R. J.; Fischer, D. A.; Gundlach, D. J.; Toney, M. F.; Richter, L. J.; DeLongchamp, D. M. Interfacial Segregation in Polymer/Fullerene Blend Films for Photovoltaic Devices. *Macromolecules* **2010**, *43*, 3828–3836.

11. Björström, C. M.; Nilsson, S.; Bernasik, A.; Budkowski, A.; Andersson, M.; Magnusson, K. O.; Moons, E. Vertical Phase Separation in Spin-Coated Films of a Low Bandgap Polyfluorene/PCBM Blend—Effects of Specific Substrate Interaction. *Appl. Surf. Sci.* **2007**, *253*, 3906–3912.

12. Keum, J. K.; Browning, J. F.; Xiao, K.; Shao, M.; Halbert, C. E.; Hong, K. Morphological Origin for the Stratification of P3HT:PCBM Blend Film Studied by Neutron Reflectometry. *Appl. Phys. Lett.* **2013**, *103*, 223301.

13. Lee, C.-K.; Wodo, O.; Ganapathysubramanian, B.; Pao, C.-W. Electrode Materials, Thermal Annealing Sequences, and Lateral/Vertical Phase Separation of Polymer Solar

Cells from Multiscale Molecular Simulations. *ACS Appl. Mater. Interfaces* **2014**, *6*, 20612–20624.

14. Alonzo, J.; Kochemba, W. M.; Pickel, D. L.; Ramanathan, M.; Sun, Z.; Li, D.; Chen, J.; Sumpter, B. G.; Heller, W. T.; Kilbey II, S. M. Assembly and Organization of Poly(3-hexylthiophene) Brushes and their Potential Use as Novel Anode Buffer Layers for Organic Photovoltaics. *Nanoscale* **2013**, *5*, 9357–9364.

15. Kim, M.; Kim, J.-H.; Choi, H. H.; Park, J. H.; Jo, S. B.; Sim, M.; Kim, J. S.; Jinnai, H.; Park, Y. D.; Cho, K. Electrical Performance of Organic Solar Cells with Additive-Assisted Vertical Phase Separation in the Photoactive Layer. *Adv. Energy Mater.* **2014**, *4*, 1300612(1)–1300612(9).

16. Yeo, J.-S.; Yun, J.-M.; Kim, D.-Y.; Park, S.; Kim, S.-S.; Yoon, M.-H.; Kim, T.-W.; Na, S.-I. Significant Vertical Phase Separation in Solvent-Vapor-Annealed Poly(3, 4-ethylenedioxythiophene): Poly(styrene sulfonate) Composite Films Leading to Better Conductivity and Work Function for High-Performance Indium Tin Oxide-Free Optoelectronics. *ACS Appl. Mater. Interfaces* **2012**, *4*, 2551–2560.

17. Yang, C.; Lee, J. K.; Heeger, A. J.; Wudl, F. Well-Defined Donor–Acceptor Rod–Coil Diblock Copolymers Based on P3HT Containing C 60: The Morphology and Role as a Surfactant in Bulk-Heterojunction Solar Cells. *J. Mater. Chem.* **2009**, *19*, 5416–5423.

18. Lee, J. U.; Jung, J. W.; Emrick, T.; Russell, T. P.; Jo, W. H. Morphology Control of a Polythiophene–Fullerene Bulk Heterojunction for Enhancement of the High-Temperature Stability of Solar Cell Performance by a New Donor–Acceptor Diblock Copolymer. *Nanotechnology* **2010**, *21*, 105201.

19. Sivula, K.; Ball, Z. T.; Watanabe, N.; Fréchet, J. M. Amphiphilic Diblock Copolymer Compatibilizers and their Effect on the Morphology and Performance of Polythiophene: Fullerene Solar Cells. *Adv. Mater.* **2006**, *18*, 206–210.

20. Lai, Y.-C.; Higashihara, T.; Hsu, J.-C.; Ueda, M.; Chen, W.-C. Enhancement of Power Conversion Efficiency and Long-Term Stability of P3HT/PCBM Solar Cells using C_{60} Derivatives with Thiophene Units as Surfactants. *Sol. Energy Mater. Sol. Cells* **2012**, *97*, 164–170.

21. Chen, J.; Yu, X.; Hong, K.; Messman, J. M.; Pickel, D. L.; Xiao, K.; Dadmun, M. D.; Mays, J. W.; Rondinone, A. J.; Sumpter, B. G.; Kilbey II, S. M. Ternary Behavior and Systematic Nanoscale Manipulation of Domain Structures in P3HT/PCBM/P3HT-b-PEO Films. *J. Mater. Chem.* **2012**, *22*, 13013–13022.

22. Deribew, D.; Pavlopoulou, E.; Fleury, G.; Nicolet, C.; Renaud, C.; Mougnier, S.-J.; Vignau, L.; Cloutet, E.; Brochon, C.; Cousin, F.; Portale, G.; Geoghegan, M.; Hadziioannou, G. Crystallization-Driven Enhancement in Photovoltaic Performance through Block Copolymer Incorporation into P3HT:PCBM Blends. *Macromolecules* **2013**, *46*, 3015–3024.

23. Sun, Z.; Xiao, K.; Keum, J. K.; Yu, X.; Hong, K.; Browning, J.; Ivanov, I. N.; Chen, J.; Alonzo, J.; Li, D.; Sumpter, B. G.; Payzant, E. A.; Rouleau, C. M.; Geohegan, D. B. PS-b-P3HT Copolymers as P3HT/PCBM Interfacial Compatibilizers for High Efficiency Photovoltaics. *Adv. Mater.* **2011**, *23*, 5529–5535.

24. Kipp, D.; Ganesan, V. Influence of Block Copolymer Compatibilizers on the Morphologies of Semiflexible Polymer/Solvent Blends. *J. Phys. Chem. B* **2014**, *118*, 4425–4441.

25. Carrillo, J.-M. Y.; Kumar, R.; Goswami, M.; Sumpter, B. G.; Brown, W. M. New Insights into the Dynamics and Morphology of P3HT:PCBM Active Layers in Bulk Heterojunctions. *Phys. Chem. Chem. Phys.* **2013**, *15*, 17873–17882.

26. Hack, J. J.; Papka, M. E. Advances in Leadership Computing. *Comput. Sci. Eng.* **2014**, *16*, 10–12.

27. Lee, C.-K.; Pao, C.-W.; Chu, C.-W. Multiscale Molecular Simulations of the Nanoscale Morphologies of P3HT:PCBM Blends for Bulk Heterojunction Organic Photovoltaic Cells. *Energy Environ. Sci.* **2011**, *4*, 4124–4132.

28. Plimpton, S. Fast Parallel Algorithms for Short-Range Molecular Dynamics. *J. Comput. Phys.* **1995**, *117*, 1–19.

29. Brown, W. M.; Wang, P.; Plimpton, S. J.; Tharrington, A. N. Implementing Molecular Dynamics on Hybrid High Performance Computers–Short Range Forces. *Comput. Phys. Commun.* **2011**, *182*, 898–911.

30. Liu, F.; Chen, D.; Wang, C.; Luo, K.; Gu, W.; Briseno, A. L.; Hsu, J. W.; Russell, T. P. Molecular Weight Dependence of the Morphology in P3HT:PCBM Solar Cells. *ACS Appl. Mater. Interfaces* **2014**, *6*, 19876–19887.

31. Kline, R. J.; McGehee, M. D.; Kadnikova, E. N.; Liu, J.; Fréchet, J. M. Controlling the Field-Effect Mobility of Regioregular Polythiophene by Changing the Molecular Weight. *Adv. Mater.* **2003**, *15*, 1519–1522.

32. Goh, C.; Kline, R. J.; McGehee, M. D.; Kadnikova, E. N.; Fréchet, J. M. Molecular-Weight-Dependent Mobilities in Regioregular Poly(3-hexyl-thiophene) Diodes. *Appl. Phys. Lett.* **2005**, *86*, 122110.

33. Chen, D.; Nakahara, A.; Wei, D.; Nordlund, D.; Russell, T. P. P3HT/PCBM Bulk Heterojunction Organic Photovoltaics: Correlating Efficiency and Morphology. *Nano Lett.* **2010**, *11*, 561–567.

34. Chen, D.; Liu, F.; Wang, C.; Nakahara, A.; Russell, T. P. Bulk Heterojunction Photovoltaic Active Layers *via* Bilayer Interdiffusion. *Nano Lett.* **2011**, *11*, 2071–2078.

35. Wu, W.-R.; Jeng, U.-S.; Su, C.-J.; Wei, K.-H.; Su, M.-S.; Chiu, M.-Y.; Chen, C.-Y.; Su, W.-B.; Su, C.-H.; Su, A.-C. Competition Between Fullerene Aggregation and Poly(3-

hexylthiophene) Crystallization upon Annealing of Bulk Heterojunction Solar Cells. *ACS Nano* **2011**, *5*, 6233–6243.

36. Flory, P. J. *Principles of Polymer Chemistry*; Baker lectures 1948; Cornell University Press, 1953.

37. Rubinstein, M.; Colby, R. *Polymer Physics*; OUP Oxford, 2003.

38. Kozub, D. R.; Vakhshouri, K.; Orme, L. M.; Wang, C.; Hexemer, A.; Gomez, E. D. Polymer Crystallization of Partially Miscible Polythiophene/Fullerene Mixtures Controls Morphology. *Macromolecules* **2011**, *44*, 5722–5726.

39. Kumar, R.; Carrillo, J.-M.; Goswami, M.; Sumpter, B. *Organic Solar Cells*; CRC Press, 2015; pp 113–140.

40. Collins, B. A.; Gann, E.; Guignard, L.; He, X.; McNeill, C. R.; Ade, H. Molecular Miscibility of Polymer- Fullerene Blends. *J. Phys. Chem. Lett.* **2010**, *1*, 3160–3166.

41. Chen, H.; Hegde, R.; Browning, J.; Dadmun, M. The Miscibility and Depth Profile of PCBM in P3HT: Thermodynamic Information to Improve Organic Photovoltaics. *Phys. Chem. Chem. Phys.* **2012**, *14*, 5635–5641.

42. Osterloh, F. E.; Holmes, M. A.; Zhao, J.; Chang, L.; Kawula, S.; Roehling, J. D.; Moulé, A. J. P3HT:PCBM Bulk-Heterojunctions: Observing Interfacial and Charge Transfer States with Surface Photovoltage Spectroscopy. *J. Phys. Chem. C* **2014**, *118*, 14723–14731.

43. Debye, P.; Anderson Jr, H.; Brumberger, H. Scattering by an Inhomogeneous Solid. II. The Correlation Function and its Application. *J. Appl. Phys.* **1957**, *28*, 679–683.

44. Fratzl, P.; Lebowitz, J. Universality of Scaled Structure Functions in Quenched Systems Undergoing Phase Separation. *Acta Metall.* **1989**, *37*, 3245–3248.

45. Rycroft, C. H. VORO++: A Three-Dimensional Voronoi Cell Library in C++. *Chaos* **2009**, *19*, 041111.

46. Scheutjens, J.; Fleer, G. In *The Effect of Polymers on Dispersion Properties*; Tadros, T. F., Ed.; Academic Press, London, 1982.

47. Kiel, J.; Mackay, M.; Kirby, B.; Maranville, B.; Majkrzak, C. Phase-Sensitive Neutron Reflectometry Measurements Applied in the Study of Photovoltaic Films. *J. Chem. Phys.* **2010**, *133*, 074902.

48. Heavens, O. S. *Optical Properties of Thin Solid Films*; Courier Dover Publications, 1991.

49. Ankner, J.; Majkrzak, C. *SPIE Conference Proceedings*; 1992; Vol. 1738; pp 260–269.

50. Russell, T. X-Ray and Neutron Reflectivity for the Investigation of Polymers. *Mater. Sci. Rep.* **1990**, *5*, 171–271.

51. Liu, H.-J.; Jeng, U.-S.; Yamada, N. L.; Su, A.-C.; Wu, W.-R.; Su, C.-J.; Lin, S.-J.; Wei, K.-H.; Chiu, M.-Y. Surface and Interface Porosity of Polymer/Fullerene-Derivative Thin Films Revealed by Contrast Variation of Neutron and X-ray Reflectivity. *Soft Matter* **2011**, *7*, 9276–9282.

52. Brédas, J.-L.; Calbert, J. P.; da Silva Filho, D.; Cornil, J. Organic Semiconductors: A Theoretical Characterization of the Basic Parameters Governing Charge Transport. *Proc. Natl. Acad. Sci. U.S.A.* **2002**, *99*, 5804–5809.

53. Lan, Y.-K.; Huang, C.-I. A Theoretical Study of the Charge Transfer Behavior of the Highly Regioregular Poly-3-Hexylthiophene in the Ordered State. *J. Phys. Chem. B* **2008**, *112*, 14857–14862.

54. Yin, W.; Dadmun, M. A New Model for the Morphology of P3HT/PCBM Organic Photovoltaics from Small-Angle Neutron Scattering: Rivers and Streams. *ACS Nano* **2011**, *5*, 4756–4768.

55. Malik, S.; Nandi, A. K. Crystallization Mechanism of Regioregular Poly(3-alkyl thiophene)s. *J. Polym. Sci., Part B: Polym. Phys.* **2002**, *40*, 2073–2085.

56. Kohn, P.; Rong, Z.; Scherer, K. H.; Sepe, A.; Sommer, M.; Müller-Buschbaum, P.; Friend, R. H.; Steiner, U.; Hüttner, S. Crystallization-Induced 10-nm Structure Formation in P3HT/PCBM Blends. *Macromolecules* **2013**, *46*, 4002–4013.

57. Wang, J.; Wolf, R. M.; Caldwell, J. W.; Kollman, P. A.; Case, D. A. Development and Testing of a General Amber Force Field. *J. Comput. Chem.* **2004**, *25*, 1157–1174.

58. To, T.; Adams, S. Modelling of P3HT:PCBM Interface Using Coarse-Grained Forcefield Derived from Accurate Atomistic Force Field. *Phys. Chem. Chem. Phys.* **2014**, *16*, 4653–4663.

59. Kohn, P.; Huettner, S.; Komber, H.; Senkovskyy, V.; Tkachov, R.; Kiriy, A.; Friend, R. H.; Steiner, U.; Huck, W. T. S.; Sommer, J.-U.; Sommer, M. On the Role of Single Regiodefects and Polydispersity in Regioregular Poly(3-hexylthiophene): Defect Distribution, Synthesis of Defect-Free Chains, and a Simple Model for the Determination of Crystallinity. *J. Am. Chem. Soc.* **2012**, *134*, 4790–4805.

60. Ismail, A. E.; Grest, G. S.; Stevens, M. J. Capillary Waves at the Liquid-Vapor Interface and the Surface Tension of Water. *J. Chem. Phys.* **2006**, *125*, 014702.

61. Sides, S. W.; Grest, G. S.; Lacasse, M.-D. Capillary Waves at Liquid-Vapor Interfaces: A Molecular Dynamics Simulation. *Phys. Rev. E: Stat., Nonlinear, Soft Matter Phys.* **1999**, *60*, 6708–6713.

62. Blas, F. J.; MacDowell, L. G.; de Miguel, E.; Jackson, G. Vapor-Liquid Interfacial Properties of Fully Flexible Lennard-Jones Chains. *J. Chem. Phys.* **2008**, *129*, 144703.

63. LeGrand, D.; Gaines, G. Surface Tension of Homologous Series of Liquids. *J. Colloid Interface Sci.* **1973**, *42*, 181–184.

64. Li, L.-H.; Kontsevoi, O. Y.; Freeman, A. J. Orientation-Dependent Electronic Structures and Optical Properties of the P3HT:PCBM Interface: A First-Principles GW-BSE Study. *J. Phys. Chem. C* **2014**, *118*, 10263–10270.

65. Marchiori, C.; Koehler, M. Density Functional Theory Study of the Dipole Across the P3HT:PCBM Complex: The Role of Polarization and Charge Transfer. *J. Phys. D: Appl. Phys.* **2014**, *47*, 215104.

66. Scharber, M. C.; Mühlbacher, D.; Koppe, M.; Denk, P.; Waldauf, C.; Heeger, A. J.; Brabec, C. J. Design Rules for Donors in Bulk-Heterojunction Solar Cells—Towards 10% Energy-Conversion Efficiency. *Adv. Mater.* **2006**, *18*, 789–794.

67. Valiev, M.; Bylaska, E.; Govind, N.; Kowalski, K.; Straatsma, T.; Dam, H. V.; Wang, D.; Nieplocha, J.; Apra, E.; Windus, T.; de Jong, W. NWChem: A Comprehensive and Scalable Open-Source Solution for Large Scale Molecular Simulations. *Comput. Phys. Commun.* **2010**, *181*, 1477 – 1489.

68. Hehre, W. J.; Ditchfield, R.; Pople, J. A. Self—Consistent Molecular Orbital Methods. XII. Further Extensions of Gaussian—Type Basis Sets for Use in Molecular Orbital Studies of Organic Molecules. *J. Chem. Phys.* **1972**, *56*, 2257–2261.

69. Nooijen, M.; Bartlett, R. J. Equation of Motion Coupled Cluster Method for Electron Attachment. *J. Chem. Phys.* **1995**, *102*, 3629–3647.

70. Stanton, J. F.; Gauss, J. Perturbative Treatment of the Similarity Transformed Hamiltonian in Equation-of-Motion Coupled-Cluster Approximations. *J. Chem. Phys.* **1995**, *103*, 1064–1076.

71. Musiał, M.; Kucharski, S. A.; Bartlett, R. J. Equation-of-Motion Coupled Cluster Method with Full Inclusion of the Connected Triple Excitations for Ionized States: IP-EOM-CCSDT. *J. Chem. Phys.* **2003**, *118*, 1128–1136.

72. Musiał, M.; Bartlett, R. J. Equation-of-Motion Coupled Cluster Method with Full Inclusion of Connected Triple Excitations for Electron-Attached States: EA-EOM-CCSDT. *J. Chem. Phys.* **2003**, *119*, 1901–1908.

73. Bhaskaran-Nair, K.; Kowalski, K.; Moreno, J.; Jarrell, M.; Shelton, W. A. Equation of Motion Coupled Cluster Methods for Electron Attachment and Ionization Potential in Fullerenes C60 and C70. *J. Chem. Phys.* **2014**, *141*, 074304.

74. Bhaskaran-Nair, K.; Kowalski, K.; Jarrell, M.; Moreno, J.; Shelton, W. A. Equation of Motion Coupled Cluster Methods for Electron Attachment and Ionization Potential in Polyacenes. *Chem. Phys. Lett.* **2015**, *641*, 146–152.

75. Bhaskaran-Nair, K.; Valiev, M.; Deng, S.; Shelton, W. A.; Kowalski, K.; Wang, X.-B. Probing Microhydration Effect on the Electronic Structure of the GFP Chromophore Anion: Photoelectron Spectroscopy and Theoretical Investigations. *J. Chem. Phys.* **2015**, *143*, 224301.

76. Liu, T.; Cheung, D. L.; Troisi, A. Structural variability and Dynamics of the P3HT/PCBM Interface and its Effects on the Electronic Structure and the Charge-Transfer Rates in Solar Cells. *Phys. Chem. Chem. Phys.* **2011**, *13*, 21461–21470.

77. Loewe, R. S.; Khersonsky, S. M.; McCullough, R. D. A Simple Method to Prepare Head-to-Tail Coupled, Regioregular Poly(3-alkylthiophenes) Using Grignard Metathesis. *Adv. Mater.* **1999**, *11*, 250–253.

78. Ahn, S.; Pickel, D. L.; Kochemba, W. M.; Chen, J.; Uhrig, D.; Hinestrosa, J. P.; Carrillo, J.-M.; Shao, M.; Do, C.; Messman, J. M.; Brown, W. M.; Sumpter, B. G.; Kilbey II, S. M. Poly(3-hexylthiophene) Molecular Bottlebrushes *via* Ring-Opening Metathesis Polymerization: Macromolecular Architecture Enhanced Aggregation. *ACS Macro Lett.* **2013**, *2*, 761–765.

79. Kochemba, W. M.; Pickel, D. L.; Sumpter, B. G.; Chen, J.; Kilbey, S. M. *In situ* Formation of Pyridyl-Functionalized Poly(3-hexylthiophene)s *via* Quenching of the Grignard Metathesis Polymerization: Toward Ligands for Semiconductor Quantum Dots. *Chem. Mater.* **2012**, *24*, 4459–4467.

80. Kochemba, W. M.; Kilbey, S. M.; Pickel, D. L. End-group Composition of Poly(3-hexylthiophene)s Prepared by *in situ* Quenching of the Grignard Metathesis Polymerization: Influence of Additives and Reaction Conditions. *J. Polym. Sci., Part A: Polym. Chem.* **2012**, *50*, 2762–2769.

Graphical TOC Entry

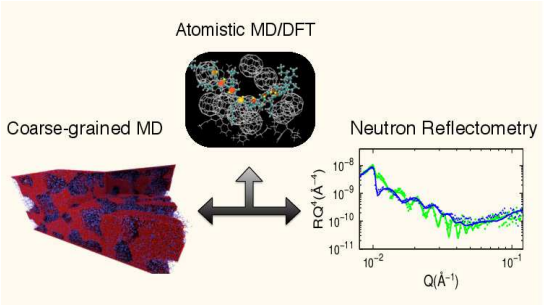

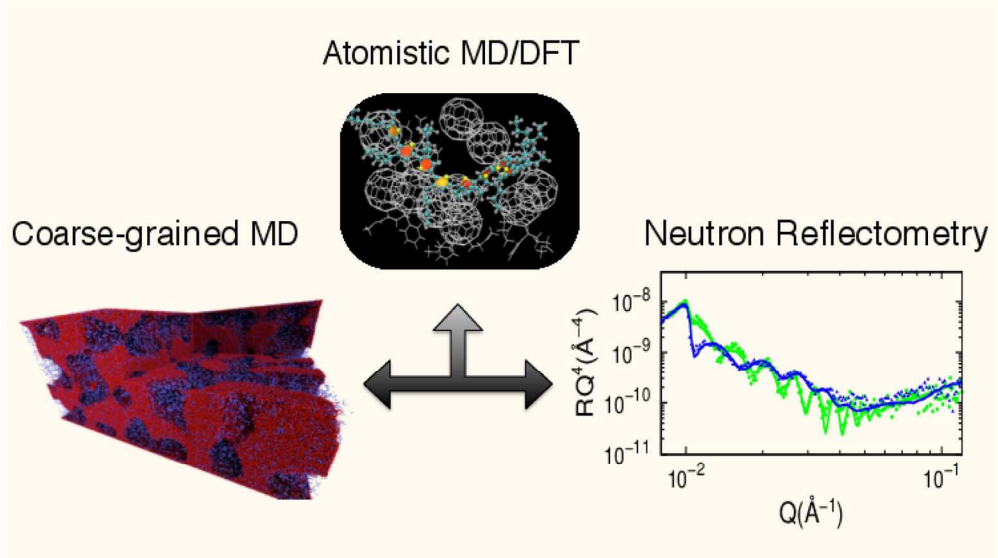

147x82mm (300 x 300 DPI)

Supporting Information for: Petascale Simulations of the Morphology and the Molecular Interface of Bulk Heterojunctions

Jan-Michael Y. Carrillo,[*,†,‡] Zach Seibers,[¶] Rajeev Kumar,[†,‡] Michael A. Matheson,[§] John F. Ankner,[‖] Monojoy Goswami,[†,‡] Kiran Bhaskaran-Nair,[⊥,#] William A. Shelton,[⊥,#] Bobby G. Sumpter,[†,‡] and S. Michael Kilbey,II[*,@]

†*Center for Nanophase Materials Sciences, Oak Ridge National Laboratory, Oak Ridge, TN 37831, USA*
‡*Computer Science and Mathematics Division, Oak Ridge National Laboratory, Oak Ridge, TN 37831, USA*
¶*Department of Energy Science and Engineering, University of Tennessee, Knoxville, TN 37996, USA*
§*National Center for Computational Sciences, Oak Ridge National Laboratory, Oak Ridge, TN 37831, USA*
‖*Spallation Neutron Source, Oak Ridge National Laboratory, Oak Ridge, TN 37831, USA*
⊥*Center for Computation and Technology, Louisiana State University, Baton Rouge, LA 70803, USA*
#*Cain Department of Chemical Engineering, Louisiana State University, Baton Rouge, LA 70803, USA*
@*Departments of Chemistry and Chemical and Biomolecular Engineering, University of Tennessee, Knoxville, TN 37996, USA*

E-mail: carrillojy@ornl.gov; mkilbey@utk.edu

Simulation Details

Coarse-grained molecular dynamics simulation details

The simulations were performed using the P3HT-PCBM coarse-grained force field developed by Lee, Pao and Chu (LPC)[1] and were ran using LAMMPS.[2] The details of the implementation of the simulations are similar to those described by Carrillo *et al.*,[3] but with the

addition of substrates (see Fig. S.1). In this work we used the results obtained by the neutron reflectometry experiments by Kiel *et al.*[4] as a reference to determine the strength of the interaction potential of P3HT and PCBM with a silicon based substrate. Kiel *et al.*[4] observed that for a BHJ thin film of 1:1 weight ratio of P3HT:PCBM in contact with a silicon wafer substrate the volume fraction of PCBM near the substrate is 75%. Accordingly, to model the bottom substrate in the simulations, we used a *diamond cubic lattice* representing the crystalline structure of silicon with the size of the substrate atoms set at 4.2 Å, which is commensurate to twice the van der Waals radius, r_w, of a silicon atom. Thereafter we estimated the mole ratio of PCBM to P3HT adsorbed in the substrate based on Boltzmann factor $e^{-U(r)/k_BT}$, where the attractive interaction potential between the substrate and either P3HT or PCBM, $U(r)$, is proportional to $-\varepsilon$ where ε is the Lennard-Jones interaction parameter. In this regard, the PCBM to P3HT mole ratio adsorbed on the substrate, m_r, is

$$m_r = \exp\left(\frac{\varepsilon_{\text{PCBM-substrate}} - \varepsilon_{\text{P3HT-substrate}}}{k_BT}\right) \tag{S.1}$$

and the PCBM mole fraction is, $x_{\text{PCBM}} = 1 - 1/(m_r + 1)$.

We took into account the size difference between the P3HT and PCBM beads and calculated the volume occupied by one P3HT or one PCBM sphere, which is equal to $V = 4\pi r^3/3\eta$ where η is the packing fraction and r is the radius of a Lennard-Jones bead at 423 K. The values of η_{PCBM} and η_{P3HT}, 0.53 and 0.42, respectively, were obtained from bulk simulations of 1:1 P3HT:PCBM mixture.[3] In one mole of a P3HT:PCBM blend adsorbed in the substrate, the volume fraction of adsorbed PCBM, $\phi_{\text{PCBM},ads}$ is expressed as

$$\phi_{\text{PCBM},ads} = \frac{x_{\text{PCBM}}V_{\text{PCBM}}}{x_{\text{PCBM}}V_{\text{PCBM}} + (1 - x_{\text{PCBM}})V_{\text{P3HT}}} \tag{S.2}$$

Finally, setting the value of $\varepsilon_{\text{PCBM-substrate}}$ equal to 0.1 kcal/mol and $\varepsilon_{\text{P3HT-substrate}}$ equal to 0.75 kcal/mol results in $\phi_{\text{PCBM},ads} = 0.753$, which is in agreement with the experiments by Kiel *et al.*[4] The top substrate is composed of purely repulsive Lennard-Jones beads

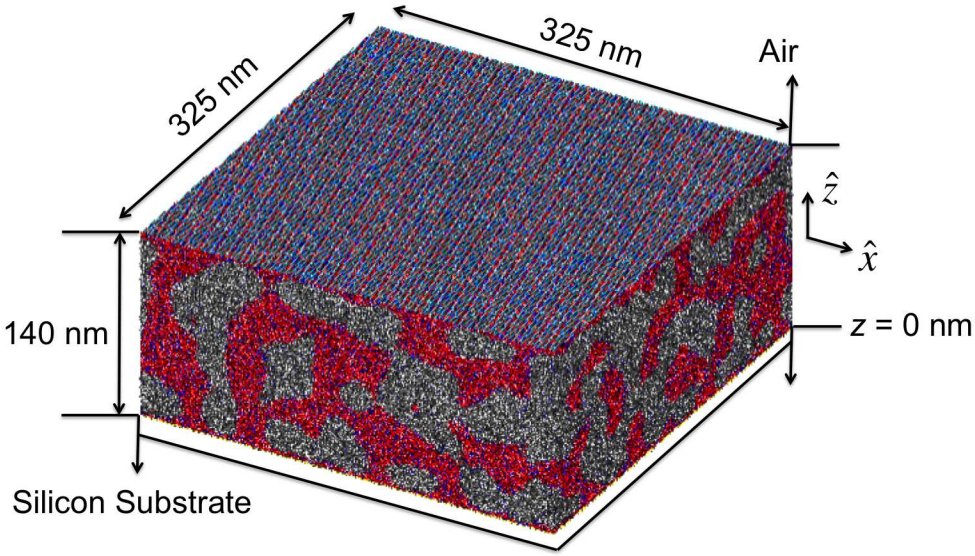

Figure S.1: Snapshot of the simulation box showing the P3HT (red) and PCBM (gray) domains. The silicon substrate and air interfaces are located at the bottom and top of the slab, respectively. The plane at $z = 0$ pertains to the location of the silicon substrate-BHJ interface. The simulation contains 71,871,869 Lennard-Jones beads.

arranged in a 2D hexagonal lattice, where the values of $\varepsilon_{\mathrm{PCBM-topsubstrate}}$ and $\varepsilon_{\mathrm{P3HT-topsubstrate}}$ arbitrarily were set to 1.0 kcal/mol ($\approx$ 1.2 k_BT). The corresponding σ_{LJ} parameter for PCBM-substrate and P3HT-substrate is determined as the arithmetic mean of the σ of its components.

The simulation box is periodic in x, y and z directions with dimensions of $L_x = L_y = 325.8$ nm and $L_z = 202.2$ nm. On each LJ bead at the film/air interface we applied a constant force directed along z axis (in the negative direction) to ensure that the density of the BHJ at the middle is equal to its bulk density. This results in the fluctuation of the top region (strata) at around $z \approx 140$ nm, and the simulation have a vacuum buffer of around 60 nm from its z periodic image. The simulation described and used here constitutes n_b = 11,520,000 bottom substrate ("silicon") beads, n_t = 2,880,000 top substrate ("air") beads and n_{TOTAL} = 71,871,869 beads total, including substrates, PCBM and P3HT.

There are four thin film systems simulated which have different distributions of mixtures of long ($N_l = 100$) and short ($N_s = 10$) P3HT chains. The overall P3HT:PCBM weight

ratio is maintained at 1:1 while the weight percentage of the short chains is systematically varied from $\phi_a = 0$ to 10%. There are constant numbers of PCBM and P3HT beads, which are $n_{\mathrm{PCBM}} = 8{,}871{,}869$ and $n_{\mathrm{P3HT}} = 48{,}600{,}000$. Table S.1 lists the number of long (m_l) and short (m_s) P3HT chains in the simulation box as the relative amount of low molecular weight P3HT oligomers, ϕ_a, is changed.

Table S.1: Number of long (m_l) and short (m_s) P3HT chains in the simulation box as a function of the relative amount of low molecular weight P3HT oligomers, ϕ_a.

ϕ_a	m_l	m_s
0.0 %	486,000	0
2.5 %	461,700	243,000
5.0 %	437,400	486,000
10.0 %	388,800	972,000

Table S.2 lists pertinent details of the simulation box for the simulations without bounding substrates (bulk configuration). There are $m_l = 9600$ long chains and the number of short chains m_s is varied to give different ϕ_a values. An appropriate amount of PCBM beads, n_{PCBM}, were added to maintain an overall P3HT:PCBM weight ratio of 1:1. At constant m_l, the addition of short P3HT chains results in an increase in the cubic simulation box dimension, L.

Table S.2: Details of the bulk simulation systems.

ϕ_a	m_l	m_s	L (nm)	n_{PCBM}	n_{TOTAL}
0.0 %	9,600	0	66.4	175,247	1,135,247
2.5 %	9,600	5,053	67.6	184,471	1,195,001
5.0 %	9,600	10,667	68.9	194,719	1,261,389
10.0 %	9,600	24,000	71.7	219,058	1,419,058
20.0 %	9,600	64,000	79.2	292,078	1,892,078

Segment alignment

It was determined by Carrillo *et al.*[3] that there are approximately 10 P3HT beads in a persistent segment in the LPC[1] model. To quantify the alignment of the persistent segments, the polymer chains were divided into segments consisting of 10 consecutive beads. In each segment, the nearest neighbor segments were determined and their unit vectors are defined as the set, $\left\{u^{(i)}\right\}$. These unit vectors are defined by the positions of the first and last bead. From the set of unit vectors, the second rank order tensor was calculated as

$$S_{\alpha\beta} = \frac{1}{N_u}\sum_{i}^{N_u}\left(u_\alpha^{(i)}u_\beta^{(i)} - \frac{1}{3}\delta_{\alpha\beta}\right) \tag{S.3}$$

where N_u is the number of vectors in $\left\{u^{(i)}\right\}$, the indexes α, $\beta = x, y, z$, and $\delta_{\alpha\beta}$ is the Kronecker delta function. The eigenvalues of the symmetric 3×3 tensor are $\left\{\frac{2}{3}S, -\frac{1}{3}S + B, -\frac{1}{3}S - B\right\}$ and are ordered in such a way that $|S|$ has the largest value. S is the order parameter, where $S = 1$ indicates perfectly aligned vectors and $S = 0$ corresponds to an isotropic system. In Figure S.2, the local order parameter $S(x, y, z)$ is plotted for $N = 100$ and $\phi_{\text{P3HT}} = 0.5$, which shows stronger alignment of the segments at the edges and regions where two domains are connected. Also, the average S was plotted as a function of the P3HT volume fraction, and the trend shows a non-monotonic behavior with maximum segment alignment at $\phi_{\text{P3HT}} \approx 0.5$. Both results show the confining effect of PCBM on the alignment of segments. The values for the smaller system with number of chains, $m = 1,200$ is oscillating and can be attributed to finite size effect due to the box not being large enough to sample the P3HT-rich domains.

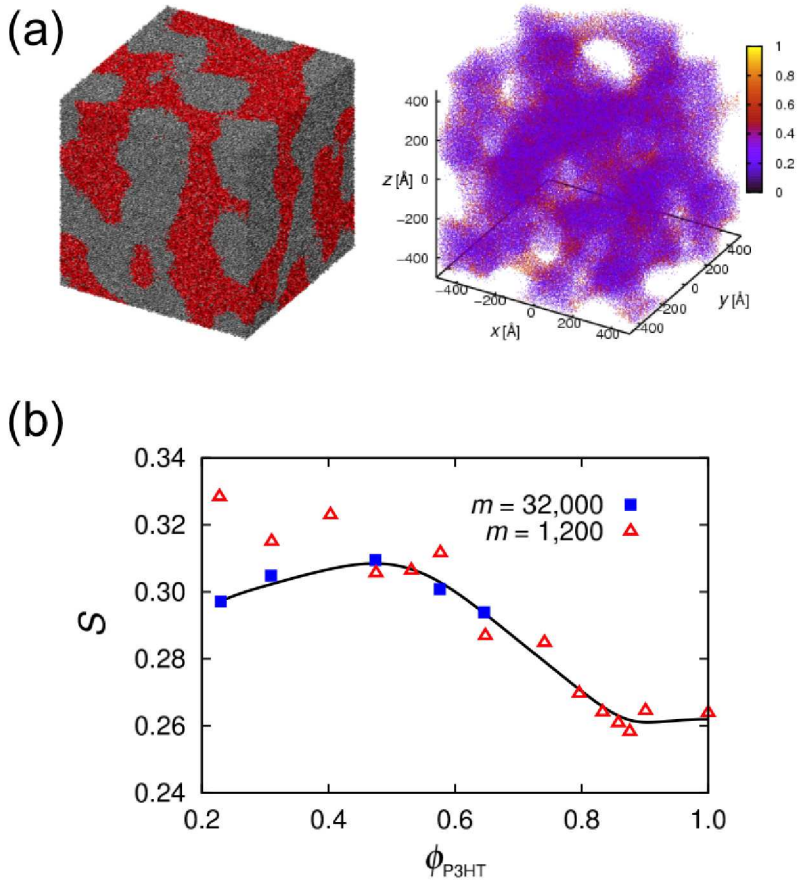

Figure S.2: (a) Local order parameter $S(x, y, z)$ of persistent segment of P3HT chains for P3HT:PCBM blends with $N = 100$ and $\phi_{\mathrm{P3HT}} = 0.5$ (b) Average order parameter, S of the persistent segments for P3HT:PCBM blends with $N = 100$ at different values of ϕ_{P3HT}. The line serves as a guide to the eye.

Volume fraction and scattering length density (SLD)

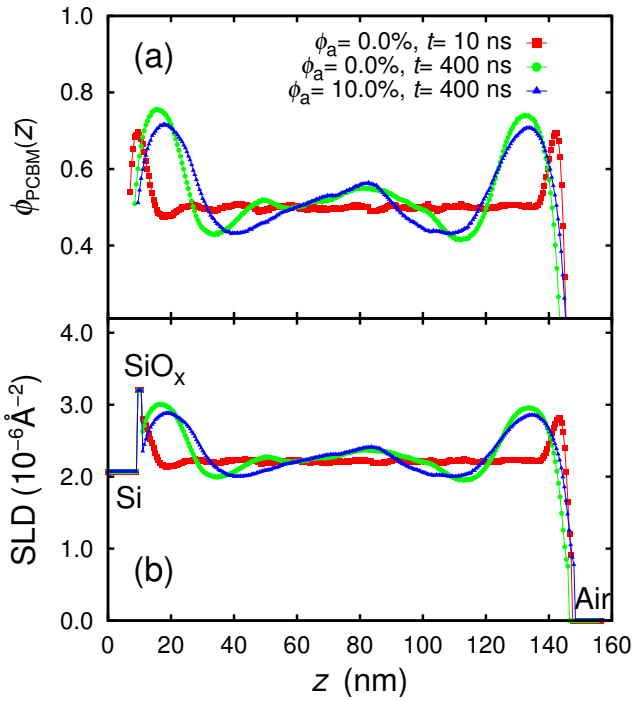

Figure S.3: (a) Laterally averaged vertical distribution of PCBM volume fraction, $\phi_{\mathrm{PCBM}}(z)$ at different t and ϕ_a in CGMD simulations. Data points for $\phi_a = 0.0\%$ and $t = 10$ ns (red squares) represents the initial conditions of the annealing process; $\phi_a = 0.0\%$ and $t = 400$ ns (green circles) and $\phi_a = 10.0\%$ and $t = 400$ ns (blue triangles) data points represent systems with and without short P3HT chains (additive) after the annealing process, respectively. (b) Scattering length densities (SLD) of the corresponding volume fraction distributions with, Si and SiO_x layers included.

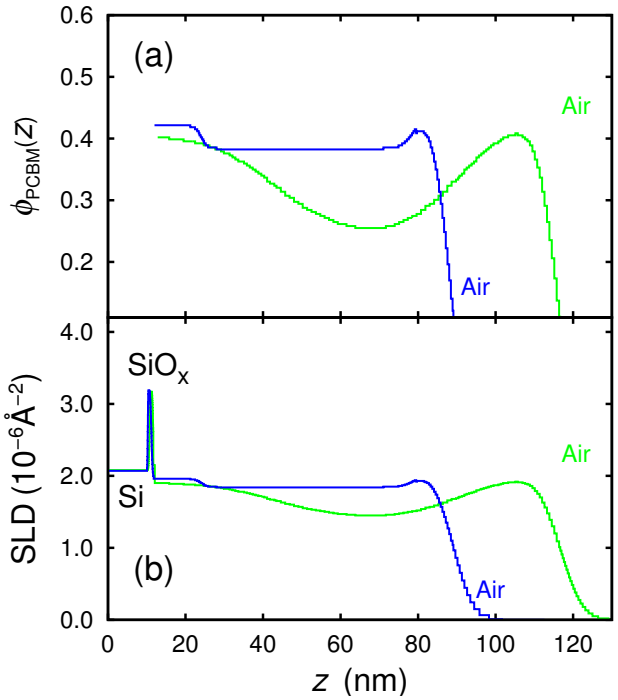

Figure S.4: Analysis of the neutron reflectivity data: (a) PCBM volume fraction, $\phi_{\mathrm{PCBM}}(z)$; and (b) Scattering length density (SLD) obtained from the fits in Figure 6(b) for the systems with (blue) and without (green) low molecular weight additive.

Table S.3: PCBM volume fraction, ϕ_{PCBM}, of the film and peak values of ϕ_{PCBM} near the interfaces and at the middle of the film obtained by fitting the data in Figure 6(b) with a three-layer model for the systems with and without low molecular weight additive (control).

ϕ_{PCBM}, Location	Control	with Additive
SiO_x-film interface	0.40 ± 0.03	0.42 ± 0.04
Middle of the film	0.26 ± 0.04	0.38 ± 0.06
Air-film interface	0.41 ± 0.02	0.41 ± 0.02
Total Film	0.31 ± 0.05	0.35 ± 0.05

Atomistic molecular dynamics simulation details

The force filed used for the atomistic MD simulation is the Generalized Amber Force Field (GAFF)[5] and the atomic partial charges are derived from the AM1/BCC routine in antechamber[6] which is a part of the AMBER package. The description of a molecule in GAFF includes long-range Coulomb and short-range van der Waals interactions, harmonic bonds, harmonic angles, and harmonic dihedrals. The total potential energy of GAFF is described by the equation

$$\begin{aligned} U_{tot} = \sum_{bonds} k_{bond}(r - r_{eq})^2 + \sum_{angles} k_{angle}(\theta - \theta_{eq})^2 \\ + \sum_{dihedrals} k_{dihedral}(1 + d\cos(n\phi)) + \sum_{1<j} \left[\frac{A_{ij}}{R_{ij}^{12}} - \frac{B_{ij}}{R_{ij}^{6}} + \frac{q_i q_j}{\varepsilon R_{ij}} \right] \end{aligned} \tag{S.4}$$

where r_{eq} and θ_{eq} are equilibration structural parameters; K_{bond}, K_{angle} and $K_{dihedral}$ are force constants; n and d are dihedral angle parameters; and A, B, q and ε are parameters that characterize the non-bonded interactions.

The simulations were performed in an isothermal-isobaric (NPT) ensemble employing a Nosè-Hoover thermo- and barostat at temperatures equal to 300 K and 423 K and atmospheric pressure using LAMMPS[2] with GPU acceleration[7] in OLCF's Titan. The equations of motion were integrated by using the velocity Verlet algorithm with a time step of 1.0 fs. The system is periodic in the x, y and z directions with dimensions 408 Å $\times$ 408 Å $\times$ 120 Å. The Particle–Particle–Paticle–Mesh (PPPM)[8] method with an accuracy of 1.0×10^{-4} and near-field cutoff set to 10.0 Å was used to account for contributions from the long-range electrostatic interactions. The simulation box was setup at a P3HT:PCBM weight ratio of 1:4 with P3HT oligomers which have 3, 6 or 9 repeat units. The simulation was run for 64 ns, and because the total system energy of the simulation saturates at around 40 ns, the final 4 ns were used for data analysis. The system sizes, which include the number of P3HT molecules (m_{P3HT}), PCBM molecules (m_{PCBM}) and the number of atoms (n_{TOTAL}) in the

simulation box, are listed in Table S.4.

Table S.4: Details of the atomistic simulation systems.

N	$\mathrm{MW}_{\mathrm{P3HT}}$ (g/mol)	$\mathrm{MW}_{\mathrm{PCBM}}$ (g/mol)	m_{P3HT}	m_{PCBM}	n_{TOTAL}
3	528.88	910.83	6,480	15,051	1,862,328
6	1027.7	910.83	3,240	14,623	1,798,744
9	1526.52	910.83	2,160	14,480	1,777,520

Coupled Cluster Methods

In equation of motion coupled cluster (EOM-CC) formalism, the excited state wavefunction is obtained by the application of the operator $R(k)$ on the ground state wavefunction,

$$|\Psi_k\rangle = R(k)e^T|\Phi\rangle \tag{S.5}$$

Here $|\Phi\rangle$ is the reference determinant; $|\Psi_0\rangle = e^T|\Phi\rangle$ is the ground state wavefunction; $R(k)$ is the excitation operator for the k-state; and T is the cluster operator, $T = \sum_n T_n$.[9–12] In commonly used CCSD method, however, T operator is truncated at bi-exciation ($T = T_1 + T_2$), where $T_1 = \sum_i \sum_a t_i^a \, a^\dagger \, i$, and $T_2 = \sum_{i<j} \sum_{a<b} t_{ij}^{ab} \, a^\dagger b^\dagger \, ji$.[13] The indices i, j, k, ... (a, b, c, ...) refer to occupied (unoccupied) one particle levels and $a^\dagger$ and i are the creation and annihilation operators, respectively. In CCSD method the unknown amplitudes, t_i^a and t_{ij}^{ab} are obtained by solving the following

$$\langle\Phi_i^a|e^{-T}He^T|\Phi\rangle = 0 \;\; \forall i, a \tag{S.6}$$

$$\langle\Phi_{ij}^{ab}|e^{-T}He^T|\Phi\rangle = 0 \;\; \forall i, j, a, b, \tag{S.7}$$

amplitude equations. Here $\langle\Phi_i^a|$ and $\langle\Phi_{ij}^{ab}|$ are singly- and doubly- excited determinants with respect to the reference determinant. The $R(k)$ operator for electron affinity variant of

EOM-CCSD method[14] is

$$R(k) = R_1 + R_2 = \sum_a r^a(k) a^\dagger + \frac{1}{2} \sum_{ab} \sum_i r_i^{ab}(k) a^\dagger b^\dagger i \tag{S.8}$$

and the operator for the ionization potential variant (IP-EOM-CCSD)[15] is

$$R(k) = \sum_i r_i(k) i + \frac{1}{2} \sum_a \sum_{ij} r_{ij}^a(k) a^\dagger j i \tag{S.9}$$

Inserting Eq.S.5 in the non-relativistic Schrödinger equation and left multiplying by e^{-T} and using similarity transformed Hamiltonian, $e^{-T} H e^T = \bar{H}; \bar{H}_N = \bar{H} - \langle \Phi | \bar{H} | \Phi \rangle$ yields,

$$\bar{H}_N R(k) | \Phi \rangle = (E_k - E_0) R(k) | \Phi \rangle \tag{S.10}$$

The above equation in matrix form is

$$\bar{\mathbf{H}}_\mathbf{N} \mathbf{R}(\mathbf{k}) = \omega_\mathbf{k} \mathbf{R}(\mathbf{k}) \tag{S.11}$$

where $\omega_k = (E_k - E_0)$ is the energy associated with electron affinity (EA) or ionization potential (IP) processes, and it can be solved using Lanczos based methods.[16,17]

DFT and Coupled Cluster calculation results

Table S.5: B3LYP results for selected $N = 3$ and $N = 6$ geometries of P3HT oligomers employing 6-31G*, 6-31++G** and 6-311++G** spherical Gaussian basis sets. The energies are given in units of eV.

$N = 3$						
	$\mathrm{IP_{HOMO}}$			$\mathrm{EA_{LUMO}}$		
z (Å)	6-31G*	6-31++G**	6-311++G**	6-31G*	6-31++G**	6-311++G**
-14.2	4.38	4.61	4.65	-1.33	-1.62	-1.66
-9.2	4.50	4.73	4.76	-1.38	-1.66	-1.70
-4.3	4.55	4.78	4.81	-1.27	-1.56	-1.60
0.9	4.52	4.74	4.78	-1.37	-1.66	-1.70
5.8	4.55	4.77	4.81	-1.33	-1.61	-1.65

$N = 6$						
	$\mathrm{IP_{HOMO}}$			$\mathrm{EA_{LUMO}}$		
z (Å)	6-31G*	6-31++G**	6-311++G**	6-31G*	6-31++G**	6-311++G**
-12.8	4.46	4.60	4.63	-1.67	-1.93	-1.97
-8.0	4.40	4.54	4.58	-1.75	-2.01	-2.05
-2.9	4.52	4.65	4.69	-1.67	-1.93	-1.97
2.0	4.10	4.24	4.27	-1.91	-2.18	-2.22
7.0	4.41	4.54	4.58	-1.73	-1.97	-2.01

Table S.6: EA/IP-EOM-CCSD results for selected $N = 3$ and $N = 6$ geometries of P3HT employing 6-31+G or 6-31G spherical Gaussian basis sets. In all calculations, core electrons were excluded from the correlation treatment. The energies are given in units of eV.

$N = 3$			$N = 6$		
z(Å)	IP-EOM-CCSD 6-31+G	EA-EOM-CCSD 6-31+G	z(Å)	IP-EOM-CCSD 6-31G	EA-EOM-CCSD 6-31G
-14.2	5.95	-0.54	-12.8	5.66	-0.53
-9.2	6.05	-0.51	-8.0	5.61	-0.39
-4.3	6.14	-0.65	-2.9	5.75	-0.52
0.9	6.09	-0.51	2.0	5.23	-0.18
5.8	6.13	-0.57	7.0	5.60	-0.42

Neutron Reflectometry

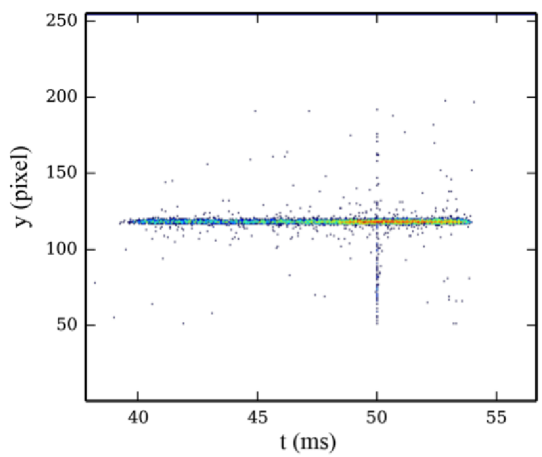

Figure S.5: Representative 2D detector image recorded for each scan used to generate the NR profiles used in this study. The y-axis corresponds to the scattering angle where $\theta = 0.5\tan^{-1}(0.7\text{mm} \times y/1350\text{mm})$ and the time of flight, t, corresponds to the wavelength of the reflected neutron $\lambda = t/0.2564$. The vertical line at $t \approx 50$ ms is due to the pulse of fast neutrons originating from the neutron source. These neutrons are filtered out as background in the data reduction process.

Approximating χ_{12} from Contact Angle Measurements

Films used in each contact angle measurement were prepared by dissolving each component in chloroform at 10 mg/mL followed by spin coating at 800 rpm for 30 s. After casting, each

film was thermally annealed at 150 °C for 15 min. under vacuum. Surface energies for each film were estimated using water and ethylene glycol contact angles and by implementing two commonly used methods to calculate the surface free energy. The first relationship used was the Neumann equation of state or the Li & Neumann model,[18] shown in Eq.S.12.

$$\cos(\theta) = -1 + 2\sqrt{\frac{\gamma_{sv}}{\gamma_{lv}}}\mathrm{e}^{-\beta(\gamma_{lv}-\gamma_{sv})^2} \tag{S.12}$$

While used in numerous sources, much debate exists surrounding the appropriate value of the coefficient β, for these calculations, $\beta = 0.0001247$ was used. As a second form of estimation, the Wu harmonic mean model,[19,20] was used to calculate the polar and dispersive components, γ^p_{sv} and γ^d_{sv}, respectively. The fact that this model features two unknown variables demands contact angle measurements using two different liquids and then simultaneously solving the two different expressions. For these measurements, water and ethylene glycol were used as probe liquids, and the respective equations are:

$$\frac{\gamma^d_{lv,\mathrm{H_2O}}\gamma^d_{sv}}{\gamma^d_{lv,\mathrm{H_2O}} + \gamma^d_{sv}} + \frac{\gamma^p_{lv,\mathrm{H_2O}}\gamma^p_{sv}}{\gamma^p_{lv,\mathrm{H_2O}} + \gamma^p_{sv}} = \frac{1}{4}\gamma_{lv,\mathrm{H_2O}}\left(1 + \cos(\theta_{\mathrm{H_2O}})\right) \tag{S.13}$$

$$\frac{\gamma^d_{lv,\mathrm{C_2H_6O_2}}\gamma^d_{sv}}{\gamma^d_{lv,\mathrm{C_2H_6O_2}} + \gamma^d_{sv}} + \frac{\gamma^p_{lv,\mathrm{C_2H_6O_2}}\gamma^p_{sv}}{\gamma^p_{lv,\mathrm{C_2H_6O_2}} + \gamma^p_{sv}} = \frac{1}{4}\gamma_{lv,\mathrm{C_2H_6O_2}}\left(1 + \cos(\theta_{\mathrm{C_2H_6O_2}})\right) \tag{S.14}$$

In equations S.12 to S.14, the following known parameters for water and ethylene glycol were used and listed in Table S.7. For the Wu model, the sum of the polar and dispersive surface energies is the average surface energy ($\gamma_{sv} = \gamma^p_{sv} + \gamma^d_{sv}$).

The calculated surface energies obtained by using the Li & Neumman and Wu models obtained from the contact angle measurements in water and ethylene glycol are summarized in Table S.8. The average of these values, $\bar{\gamma}_{sv}$, is used to compute the χ_{12} parameter between the low- and high-MW P3HT with PCBM. This was done by using the solubility parameter, δ_i, and by applying regular solution theory as shown in Eq.S.15,

Table S.7: Surface tension of water (H_2O) and ethylene glycol ($C_2H_6O_2$) used in the Neumann equation of state and the total surface tension and the polar and disperse components of the liquids used for the Wu model.

	Li & Neumann Model	Wu Model		
	γ_{lv} (mN/m)	γ_{lv} (mN/m)	γ_{lv}^{p} (mN/m)	γ_{lv}^{d} (mN/m)
H_2O	72.8[18]	72.8[21]	51.0	21.8
$C_2H_6O_2$	48.0[18]	48.2[22]	29.3	18.9

$$\chi_{ij} = \frac{V_{ij}}{RT}(\delta_i - \delta_j)^2 + \chi_{ij}^{ent} \tag{S.15}$$

where V_{ij} is the geometric mean of the component unit molar volumes and χ_{ij}^{ent} is the entropic contribution which was set to 0.34 for the polymer-PCBM pairs.[23] A first-level approximation utilizing a proportionality constant C such that $\delta_i = C\sqrt{\gamma_i}$ was used to convert surface energies, γ_i, to solubility parameters, δ_i.[24] C was set to 3.97 so as to match $\delta_{\text{PCBM}} = 22$ MPa$^{1/2}$ obtained form binary solvent gradient methods.[25] The solubility parameters, δ_i, and molar volumes, V_i, used to calculate the χ_{12} parameters of low- and high-MW P3HT with PCBM are listed in Table S.9.

Table S.8: Contact angle measurements of thermally annealed low- and high-MW P3HT and PCBM in water (H_2O) and ethylene glycol ($C_2H_6O_2$). The surface energies are calculated using the Wu Model and the Neumann Equation of State.

	Contact Angle		Li & Neumann Model		Wu Model			Average
	H_2O (deg)	$C_2H_6O_2$ (deg)	γ_{sv,H_2O} (mN/m)	$\gamma_{sv,C_2H_6O_2}$ (mN/m)	γ_{sv}^{d} (mN/m)	γ_{sv}^{p} (mN/m)	γ_{sv} (mN/m)	$\bar{\gamma}_{sv}$ (mN/m)
P3HT (5.6k)	92.1	62.2	27.88	28.39	28.33	6.75	34.98	30.4
P3HT (30k)	87.0	61.8	31.07	28.58	31.97	7.16	39.13	32.9
PCBM	93.4	58.9	27.08	29.93	28.44	6.77	35.21	30.7

Table S.9: Solubility parameters, δ_i, and molar volumes, V_i, used to calculate the χ_{12} parameters at 150 °C of low- and high-MW P3HT with PCBM.

	δ_i (MPa$^{1/2}$)	V_i[26] (cm^3/mol)	χ_{12}
P3HT (5.6k)	21.9	151	0.341
P3HT (30k)	22.8	151	0.391
PCBM	22.0	607	

References

(1) Lee, C.-K.; Pao, C.-W.; Chu, C.-W. Multiscale Molecular Simulations of the Nanoscale Morphologies of P3HT:PCBM Blends for Bulk Heterojunction Organic Photovoltaic Cells. *Energy Environ. Sci.* **2011**, *4*, 4124–4132.

(2) Plimpton, S. Fast Parallel Algorithms for Short-Range Molecular Dynamics. *J. Comput. Phys.* **1995**, *117*, 1–19.

(3) Carrillo, J.-M. Y.; Kumar, R.; Goswami, M.; Sumpter, B. G.; Brown, W. M. New Insights into the Dynamics and Morphology of P3HT:PCBM Active Layers in Bulk Heterojunctions. *Phys. Chem. Chem. Phys.* **2013**, *15*, 17873–17882.

(4) Kiel, J. W.; Kirby, B. J.; Majkrzak, C. F.; Maranville, B. B.; Mackay, M. E. Nanoparticle Concentration Profile in Polymer-Based Solar Cells. *Soft Matter* **2010**, *6*, 641–646.

(5) Wang, J.; Wolf, R. M.; Caldwell, J. W.; Kollman, P. A.; Case, D. A. Development and Testing of a General Amber Force Field. *J. Comput. Chem.* **2004**, *25*, 1157–1174.

(6) Wang, J.; Wang, W.; Kollman, P. A.; Case, D. A. Antechamber: An Accessory Software Package for Molecular Mechanical Calculations. *J. Am. Chem. Soc.* **2001**, *222*, U403.

(7) Brown, W. M.; Wang, P.; Plimpton, S. J.; Tharrington, A. N. Implementing Molecular Dynamics on Hybrid High Performance Computers–Short Range Forces. *Comput. Phys. Commun.* **2011**, *182*, 898–911.

(8) Hockney, R. W.; Eastwood, J. W. *Computer Simulation Using Particles*; CRC Press, 1988.

(9) Coester, F. Bound States of a Many-Particle System. *AIP Conf. Proc.* **1958**, *7*, 421–424.

(10) Coester, F.; Kümmel, H. Short-Range Correlations in Nuclear Wave Functions. *AIP Conf. Proc.* **1960**, *17*, 477–485.

(11) Čížek, J. On the Correlation Problem in Atomic and Molecular Systems. Calculation of Wavefunction Components in Ursell-Type Expansion Using Quantum-Field Theoretical Methods. *J. Chem. Phys.* **1966**, *45*, 4256–4266.

(12) Paldus, J.; Čížek, J.; Shavitt, I. Correlation Problems in Atomic and Molecular Systems. IV. Extended Coupled-Pair Many-Electron Theory and Its Application to the BH3 Molecule. *Phys. Rev. A* **1972**, *5*, 50.

(13) Purvis III, G. D.; Bartlett, R. J. A Full Coupled-Cluster Singles and Doubles Model: The Inclusion of Disconnected Triples. *J. Chem. Phys.* **1982**, *76*, 1910–1918.

(14) Nooijen, M.; Bartlett, R. J. Equation of Motion Coupled Cluster Method for Electron Attachment. *J. Chem. Phys.* **1995**, *102*, 3629–3647.

(15) Stanton, J. F.; Gauss, J. Perturbative Treatment of the Similarity Transformed Hamiltonian in Equation-of-Motion Coupled-Cluster Approximations. *J. Chem. Phys.* **1995**, *103*, 1064–1076.

(16) Davidson, E. R. The Iterative Calculation of a Few of the Lowest Eigenvalues and Corresponding Eigenvectors of Large Real-Symmetric Matrices. *J. Comput. Phys.* **1975**, *17*, 87–94.

(17) Hirao, K.; Nakatsuji, H. A Generalization of the Davidson's Method to Large Nonsymmetric Eigenvalue Problems. *J. Comput. Phys.* **1982**, *45*, 246–254.

(18) Li, D.; Neumann, A. Contact Angles on Hydrophobic Solid Surfaces and Their Interpretation. *J. Colloid Interface Sci.* **1992**, *148*, 190–200.

(19) Wu, S. Polar and Nonpolar Interactions in Adhesion. *J. Adhesion* **1973**, *5*, 39–55.

(20) Bulliard, X.; Ihn, S.-G.; Yun, S.; Kim, Y.; Choi, D.; Choi, J.-Y.; Kim, M.; Sim, M.; Park, J.-H.; Choi, W.; Cho, K. Enhanced Performance in Polymer Solar Cells by Surface Energy Control. *Adv. Funct. Mater.* **2010**, *20*, 4381–4387.

(21) Angellier, H.; Molina-Boisseau, S.; Belgacem, M. N.; Dufresne, A. Surface Chemical Modification of Waxy Maize Starch Nanocrystals. *Langmuir* **2005**, *21*, 2425–2433.

(22) Jańczuk, B.; Białopiotrowicz, T.; Wójcik, W. The Components of Surface Tension of Liquids and Their Usefulness in Determinations of Surface Free Energy of Solids. *J. Colloid Interface Sci.* **1989**, *127*, 59–66.

(23) Brandrup, J.; Immergut, E. H.; Grulke, E. A.; Abe, A.; Bloch, D. R. *Polymer Handbook*; Wiley New York, 1999; Vol. 89.

(24) Kipp, D.; Mok, J.; Strzalka, J.; Darling, S. B.; Ganesan, V.; Verduzco, R. Rational Design of Thermally Stable, Bicontinuous Donor/Acceptor Morphologies with Conjugated Block Copolymer Additives. *ACS Macro Lett.* **2015**, *4*, 867–871.

(25) Machui, F.; Langner, S.; Zhu, X.; Abbott, S.; Brabec, C. J. Determination of the P3HT: PCBM Solubility Parameters *via* a Binary Solvent Gradient Method: Impact of Solubility on the Photovoltaic Performance. *Sol. Energ. Mater. Sol. Cells* **2012**, *100*, 138–146.

(26) Kozub, D. R.; Vakhshouri, K.; Orme, L. M.; Wang, C.; Hexemer, A.; Gomez, E. D. Polymer Crystallization of Partially Miscible Polythiophene/Fullerene Mixtures Controls Morphology. *Macromolecules* **2011**, *44*, 5722–5726.